A phase field model for cohesive fracture in micropolar continua

Hyoung Suk Suh[a], WaiChing Sun[a,*], Devin T. O'Connor[b]

[a] *Department of Civil Engineering and Engineering Mechanics, Columbia University, 614 SW Mudd, Mail Code: 4709, New York, NY 10027, United States*
[b] *Sea Ice Research Center (SIRC) Cold Regions Research and Engineering Laboratory (CRREL) 72 Lyme Rd Hanover, NH 03755, United States*

Abstract

While crack nucleation and propagation in the brittle or quasi-brittle regime can be predicted via variational or material-force-based phase field fracture models, these models often assume that the underlying elastic response of the material is not size-dependent. Yet, a length scale parameter must be introduced to these models to enable sharp cracks properly represented by a regularized implicit function. However, many materials with internal microstructures that contain surface tension, micro-cracks, micro-fracture, inclusion, cavity or those of particulate nature often exhibit size-dependent behaviors in both the path-independent and path-dependent regimes. This paper is intended to introduce a unified treatment that captures the size effect of the materials in both elastic and damaged states. By introducing a cohesive micropolar phase field fracture theory, along with the computational model and validation exercises, we explore the interacting size-dependent elastic deformation and fracture mechanisms exhibits in materials of complex microstructures. To achieve this goal, we introduce the distinctive degradation functions of the force-stress–strain and couple-stress-micro-rotation energy-conjugated pairs for a given regularization profile such that the macroscopic size-dependent responses of the micropolar continua are insensitive to the length scale parameter of the regularized interface. Then, we apply the variational principle to derive governing equations from the micropolar stored energy and dissipative functionals. Numerical examples are introduced to demonstrate the proper way to identify material parameters and the capacity of the new formulation to simulate complex crack patterns in the quasi-static regime.
© 2020 Elsevier B.V. All rights reserved.

Keywords: Micropolar damage; Phase field fracture; Cohesive fracture; Regularization length sensitivity

1. Introduction

The size effect and the corresponding length scale parameter associated with the phase field fracture model for brittle or quasi-brittle materials have been a subject of intensive research in recent years [1–11]. Due to the fact that the phase field approach employs regularized (smoothed) implicit function to represent sharp interface, the physical interpretation of the length scale parameter (and in some cases, the lack thereof) has become a hotly debated topic among the computational fracture mechanics community. The lack of consensus on the definition of length scale has also been sometimes perceived as a weakness, especially when compared with the embedded discontinuity approaches such as XFEM or assumed strain models [12–16].

---

* Corresponding author.
  E-mail address: wsun@columbia.edu (W. Sun).

The early attempt to justify the introduction of the length scale parameter for phase field fracture models can be tracked back to the first variational fracture model in [1] where the variational fracture model is expected to exhibit $\Gamma-$convergence and therefore may converge to the sharp interface model as the mesh size and the length scale parameter approaches zero. While this line of work (e.g., [2,17]) provides a theoretical justification, in practice, the length scale parameter must still be sufficiently large compared to the mesh size in order to solve the phase field governing equation. This could be problematic if the simulations are designed for boundary value problems at the large scales (e.g., hydraulic fracture, faulting of geological formation) where the small mesh size, even concentrated at a local regions, become impractical.

One strategy to overcome this issue is to decouple or eliminate the effect of the length scale parameters on the constitutive responses such that a relatively large length scale parameter can be used for numerical purposes without compromising the accuracy of the constitutive responses. To derive a phase field fracture model that exhibits macroscopic responses independent or at least not sensitive to the length scale parameters, Wu and Nguyen [6] and Geelen et al. [18] both introduce new crack surface density functionals and the corresponding degradation function derived from cohesive zone models such that the underlying traction-separation law is independent of the length scale parameter. Their simulations have shown that the resultant fracture patterns and the macroscopic constitutive responses are both insensitive to the length scale parameters in the sub-critical regime.

Another strategy to circumvent the length scale issue is to determine the underlying relationship among the length scale parameters and other material parameters (e.g., Young's modulus, tensile strength) that can be obtained from a specific set of experimental tests [19–21]. However, these previous works also show that the analytical expression of the length scale parameter may vary in according to the chosen inverse problems and hence the length scale parameter is likely only valid for backward calibration for a specific problem but cannot be used for general-purposed forward predictions. Furthermore, identifying the correct length scale parameter for a given inverse problem does not imply that such a length scale parameter is sufficiently large to ensure the solvability of the discretized governing equation(s).

Nevertheless, *one key aspect often overlooked in the phase field fracture models is that materials with internal structures that manifest size effects on damage and fracture may likely exhibit size effect in the elastic regime*. Examples of these materials include concrete, composite, particulate materials as well as metamaterials [22–26]. Since these materials exhibit large internal length scales compared to the length scale of damage or fracture, suitable size effect must be carefully incorporated in *both* the elastic and path-dependent regimes. This paper is the first attempt to formulate a new cohesive micropolar phase field fracture theory that leads to a physically justified/identifiable size-dependent effect for both the path-independent elastic responses and the path-dependent damage and fracture in a higher-order continuum undergoing infinitesimal deformation. By extending the length-scale-parameter insensitive formulation that approximates cohesive-type of response to the micropolar materials, we introduce a third strategy where one may employ sufficiently large phase field length scale parameters to address the numerical needs without comprising the correct physical size effect that should have exhibited in the numerical simulations. In other words, the resultant model may replicate a consistent size effect for both the elastic and damage regimes, while retaining the convenience of the phase field models documented in in [6,18,27].

The rest of the paper is organized as follows. We first briefly summarize the theory of micropolar elasticity (Section 2), and introduce the strain energy split approach that enables one to explore the effects of the partitioned energy densities. We then extend the regularized length-scale-insensitive phase field formulation to the micropolar material models such that the length scale parameter for the phase field is insensitive to the macroscopic responses. This treatment then enables us to replicate the size effect characterized by the higher-order material parameters (e.g., bending and torsion stiffnesses) that can be experimentally sought. Furthermore, by enforcing the macroscopic responses not sensitive to the phase field length scale parameter, it enables us to conduct simulations in a spatial domain without the size constraint imposed by the ratio between the phase field length scale and mesh. For completeness, the details of the finite element discretization and operator-split solution scheme are discussed. Numerical examples are given to verify the implementation, provide evidences on how micropolarity affects the macroscopic behaviors for quasi-brittle materials, and showcase the applicability of the proposed models.

As for notations and symbols, bold-faced and blackboard bold-faced letters denote tensors (including vectors which are rank-one tensors); the symbol '·' denotes a single contraction of adjacent indices of two tensors (e.g., $\boldsymbol{a} \cdot \boldsymbol{b} = a_i b_i$ or $\boldsymbol{c} \cdot \boldsymbol{d} = c_{ij} d_{jk}$); the symbol ':' denotes a double contraction of adjacent indices of tensor of rank two or higher (e.g., $\mathbb{C} : \boldsymbol{\varepsilon} = C_{ijkl} \varepsilon_{kl}$); the symbol '⊗' denotes a juxtaposition of two vectors (e.g., $\boldsymbol{a} \otimes \boldsymbol{b} = a_i b_j$) or two
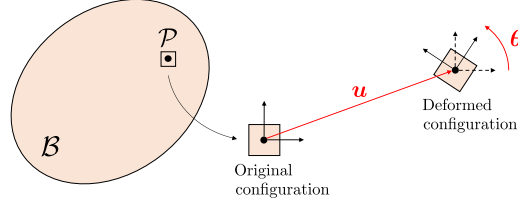
Fig. 1. Kinematics of a micropolar continuum.

symmetric second order tensors [e.g., $(\boldsymbol{\alpha} \otimes \boldsymbol{\beta})_{ijkl} = \alpha_{ij}\beta_{kl}$]. We also define identity tensors: $\boldsymbol{I} = \delta_{ij}$, $\mathbb{I} = \delta_{ik}\delta_{jl}$, and $\bar{\mathbb{I}} = \delta_{il}\delta_{jk}$, where δ_{ij} is the Kronecker delta. As for sign conventions, unless specified, the directions of the tensile stress and dilative pressure are considered as positive.

2. Theory of micropolar elasticity

In this section, we briefly summarize the kinematic and constitutive relations of an isotropic micropolar elastic materials undergoing infinitesimal deformation. In this case, the kinematics of micropolar materials is characterized by both the displacement field and the micro-rotations. The resultant strain tensor is no longer symmetric due to the higher-order kinematics. We thus decompose the strain tensor into symmetric and skew-symmetric parts, which consequently enables us to split the stored energy density into three different parts. This energy split approach opens the door for us to explore the effects of distinct degradation of partitioned energy conjugated pairs, which will be discussed later in this study.

2.1. Kinematics

Let us consider a micropolar elastic body $\mathcal{B} \subset \mathbb{R}^3$ with material points $\mathcal{P}$ identified by the position vectors $\boldsymbol{x} \in \mathcal{B}$ that undergoes infinitesimal deformation. As illustrated in Fig. 1, unlike the classical non-polar (Boltzmann) approach, each material point experiences micro-rotation $\boldsymbol{\theta}(\boldsymbol{x}, t)$, in addition to the translational displacement $\boldsymbol{u}(\boldsymbol{x}, t)$ at time t. The micro-rotation represents the local rotation of the material point $\boldsymbol{x}$, which is independent of the displacement field. Consequently, the rotational part of the polar decomposition of the displacement gradient (i.e., macro-rotation) is also independent of the micro-rotation. The micropolar strain $\bar{\boldsymbol{\varepsilon}}$ and micro-curvature $\bar{\boldsymbol{\kappa}}$ can be defined as follows [28–33]:

$$\bar{\boldsymbol{\varepsilon}} = \nabla\boldsymbol{u}^{\mathrm{T}} - \overset{3}{\boldsymbol{E}} \cdot \boldsymbol{\theta}, \tag{1}$$

$$\bar{\boldsymbol{\kappa}} = \nabla\boldsymbol{\theta}, \tag{2}$$

where $\overset{3}{\boldsymbol{E}} = \overset{3}{E}_{ijk}$ is the Levi-Civita permutation tensor. The definition of micropolar strain in Eq. (1) implies that the normal strains (i.e., diagonal entries of the micropolar strain tensor) that contribute to the stretching are equivalent to those in the classical approach, whereas the shear strains (i.e., off-diagonal entries of the micropolar strain tensor) are dependent on the micro-rotation. Since the micropolar strain tensor is non-symmetric, we therefore decompose the micropolar strain tensor into symmetric ($\bar{\boldsymbol{\varepsilon}}^{\mathrm{sym}}$) and skew-symmetric parts ($\bar{\boldsymbol{\varepsilon}}^{\mathrm{skew}}$), i.e.,

$$\bar{\boldsymbol{\varepsilon}} = \underbrace{\frac{1}{2}(\nabla\boldsymbol{u} + \nabla\boldsymbol{u}^{\mathrm{T}})}_{:=\bar{\boldsymbol{\varepsilon}}^{\mathrm{sym}}} + \underbrace{\frac{1}{2}(\nabla\boldsymbol{u}^{\mathrm{T}} - \nabla\boldsymbol{u}) - \overset{3}{\boldsymbol{E}} \cdot \boldsymbol{\theta}}_{:=\bar{\boldsymbol{\varepsilon}}^{\mathrm{skew}}}. \tag{3}$$

Notice that $\bar{\boldsymbol{\varepsilon}}^{\mathrm{sym}}$ is equivalent to the Boltzmann strain tensor in classical non-polar approach.

2.2. Constitutive model and strain energy split

To ensure stable elastic responses, the micropolar strain energy must fulfill strong ellipticity condition. To fulfill this requirement, we consider a micropolar strain energy density $\psi_e(\bar{\boldsymbol{\varepsilon}}, \bar{\boldsymbol{\kappa}})$ that takes a quadratic form:

$$\psi_e(\bar{\boldsymbol{\varepsilon}}, \bar{\boldsymbol{\kappa}}) = \frac{1}{2}\bar{\boldsymbol{\varepsilon}} : \mathbb{C} : \bar{\boldsymbol{\varepsilon}} + \frac{1}{2}\bar{\boldsymbol{\kappa}} : \mathbb{D} : \bar{\boldsymbol{\kappa}}. \tag{4}$$

Here, $\mathbb{C}$ and $\mathbb{D}$ are constitutive moduli that possess the major symmetry (i.e., $\mathbb{C} = C_{ijkl} = C_{klij}$, and $\mathbb{D} = D_{ijkl} = D_{klij}$):

$$\mathbb{C} = \lambda (\boldsymbol{I} \otimes \boldsymbol{I}) + (\mu + \kappa) \mathbb{I} + \mu \bar{\mathbb{I}} \; ; \quad \mathbb{D} = \alpha (\boldsymbol{I} \otimes \boldsymbol{I}) + \beta \bar{\mathbb{I}} + \gamma \mathbb{I}, \tag{5}$$

where λ, μ, κ, α, β, and γ are the material constants. The strong ellipticity of the strain energy density defined in Eq. (4) implies that the following inequalities must be held [31,34,35]:

$$\begin{aligned} &3\lambda + 2\mu + \kappa \geq 0 \,; \quad 2\mu + \kappa \geq 0 \,; \quad \kappa \geq 0 \,; \\ &3\alpha + \beta + \gamma \geq 0 \,; \quad \gamma + \beta \geq 0 \,; \quad \gamma - \beta \geq 0. \end{aligned} \tag{6}$$

These material constants, including the size-dependent ones are related to the following material parameters that have been individually identified via experiments [32,36,37]:

$$\begin{cases} E = \dfrac{(2\mu + \kappa)(3\lambda + 2\mu + \kappa)}{2\lambda + 2\mu + \kappa} & \text{Young's modulus,} \\[2mm] G = \dfrac{2\mu + \kappa}{2} & \text{shear modulus,} \\[2mm] \nu = \dfrac{\lambda}{2\lambda + 2\mu + \kappa} & \text{Poisson's ratio,} \\[2mm] l_t = \sqrt{\dfrac{\beta + \gamma}{2\mu + \kappa}} & \text{characteristic length in torsion,} \\[2mm] l_b = \sqrt{\dfrac{\gamma}{2(2\mu + \kappa)}} & \text{characteristic length in bending,} \\[2mm] \chi = \dfrac{\beta + \gamma}{\alpha + \beta + \gamma} & \text{polar ratio,} \\[2mm] N = \sqrt{\dfrac{\kappa}{2(\mu + \kappa)}} & \text{coupling number, } N \in [0, 1]. \end{cases} \tag{7}$$

The relations in Eq. (7) indicate that the size-dependence of the elasticity responses are related to the higher-order kinematics and kinetic. Although identification of the material parameters that characterize the size effect remains challenging as demonstrated in [38,39], these micropolar material parameters are obtainable through well-documented inverse problems or analytical solutions, at least for a subset of micropolar materials such as porous media [38]. This unambiguity is helpful for practical purposes.

In Eq. (7), the characteristic lengths l_t and l_b imply the nonlocal nature of micropolar material by quantifying the range of couple stress through their relationship to the micro-curvature. The coupling number N, on the other hand, quantifies level of shear stress asymmetry that represents the degree of micropolarity of the material, e.g., $N = 0$ corresponds to the classical elasticity while $N = 1$ corresponds to the couple-stress theory [40–42]. In the remainder of this paper, unless specified, we set $N = 0.5$ for micropolar continuum simulations.

Since this study aims to develop a framework that explores the interaction between size-dependent micropolar elasticity and fracture mechanisms, we split the strain energy density into three different parts [based on the decomposition of the micropolar strain, cf. Eq. (3)]: (1) the Boltzmann part $\psi_e^B(\bar{\boldsymbol{\varepsilon}}^{\text{sym}})$; (2) the micro-continuum coupling part $\psi_e^C(\bar{\boldsymbol{\varepsilon}}^{\text{skew}})$; and (3) the pure micro-rotational part $\psi_e^R(\bar{\boldsymbol{\kappa}})$, i.e.,

$$\psi_e(\bar{\boldsymbol{\varepsilon}}, \bar{\boldsymbol{\kappa}}) = \psi_e^B(\bar{\boldsymbol{\varepsilon}}^{\text{sym}}) + \psi_e^C(\bar{\boldsymbol{\varepsilon}}^{\text{skew}}) + \psi_e^R(\bar{\boldsymbol{\kappa}}), \tag{8}$$

where the partitioned strain energy densities can be written as:

$$\psi_e^B(\bar{\boldsymbol{\varepsilon}}^{\text{sym}}) = \frac{1}{2}\left[\lambda(\bar{\boldsymbol{\varepsilon}}^{\text{sym}} : \boldsymbol{I})^2 + (2\mu + \kappa)\,\bar{\boldsymbol{\varepsilon}}^{\text{sym}} : \bar{\boldsymbol{\varepsilon}}^{\text{sym}}\right], \tag{9}$$

$$\psi_e^C(\bar{\boldsymbol{\varepsilon}}^{\text{skew}}) = \frac{1}{2}\kappa\bar{\boldsymbol{\varepsilon}}^{\text{skew}} : \bar{\boldsymbol{\varepsilon}}^{\text{skew}}, \tag{10}$$

$$\psi_e^R(\bar{\boldsymbol{\kappa}}) = \frac{1}{2}\left[\alpha(\bar{\boldsymbol{\kappa}} : \boldsymbol{I})^2 + \beta\bar{\boldsymbol{\kappa}} : \bar{\boldsymbol{\kappa}}^{\text{T}} + \gamma\bar{\boldsymbol{\kappa}} : \bar{\boldsymbol{\kappa}}\right]. \tag{11}$$

The force stress $\bar{\boldsymbol{\sigma}}$ can be found by taking partial derivative of the energy density with respect to the micropolar strain. By using Eq. (3), the force stress can also be partitioned into $\bar{\boldsymbol{\sigma}}^B$ and $\bar{\boldsymbol{\sigma}}^C$, which are the results of the pure

non-polar deformation and the micro-continuum coupling effects, respectively:

$$\bar{\boldsymbol{\sigma}} = \frac{\partial \psi_e}{\partial \bar{\boldsymbol{\varepsilon}}} = \frac{\partial}{\partial \bar{\boldsymbol{\varepsilon}}}(\psi_e^B + \psi_e^C) = \underbrace{\lambda(\bar{\boldsymbol{\varepsilon}}^{\mathrm{sym}} : \boldsymbol{I})\boldsymbol{I} + (2\mu + \kappa)\,\bar{\boldsymbol{\varepsilon}}^{\mathrm{sym}}}_{:=\bar{\sigma}^B} + \underbrace{\kappa\bar{\boldsymbol{\varepsilon}}^{\mathrm{skew}}}_{:=\bar{\sigma}^C}. \tag{12}$$

Similarly, the couple stress $\bar{\boldsymbol{m}}^R$ that is caused by the pure micro-rotation can be obtained as follows:

$$\bar{\boldsymbol{m}}^R = \frac{\partial \psi_e}{\partial \bar{\boldsymbol{\kappa}}} = \frac{\partial \psi_e^R}{\partial \bar{\boldsymbol{\kappa}}} = \alpha(\bar{\boldsymbol{\kappa}} : \boldsymbol{I})\boldsymbol{I} + \beta\bar{\boldsymbol{\kappa}}^{\mathrm{T}} + \gamma\bar{\boldsymbol{\kappa}}. \tag{13}$$

Based on the split approach, notice that the partitioned energy densities in Eqs. (9)–(11) can be recovered by:

$$\psi_e^B = \frac{1}{2}\bar{\boldsymbol{\sigma}}^B : \bar{\boldsymbol{\varepsilon}}^{\mathrm{sym}} \; ; \; \psi_e^C = \frac{1}{2}\bar{\boldsymbol{\sigma}}^C : \bar{\boldsymbol{\varepsilon}}^{\mathrm{skew}} \; ; \; \psi_e^R = \frac{1}{2}\bar{\boldsymbol{m}}^R : \bar{\boldsymbol{\kappa}}, \tag{14}$$

where $(\bar{\boldsymbol{\sigma}} = \bar{\boldsymbol{\sigma}}^B + \bar{\boldsymbol{\sigma}}^C, \bar{\boldsymbol{\varepsilon}} = \bar{\boldsymbol{\varepsilon}}^{\mathrm{sym}} + \bar{\boldsymbol{\varepsilon}}^{\mathrm{skew}})$ and $(\bar{\boldsymbol{m}}^R, \bar{\boldsymbol{\kappa}})$ are the energy-conjugated pairs. This partition of energy then provides a mean to introduce different degradation mechanisms for different kinematic modes.

3. Phase field model for damaged micropolar continua

This section presents a variational phase field framework to model cohesive fracture in micropolar materials. Our starting point is the energy split introduced in Section 2. We introduce distinct degradation for the Boltzmann, coupling and micro-rotational energy-conjugated pairs and derive, for the first time, the action functional for the variational phase field fracture framework for micropolar continua. The governing equations are then sought by seeking the stationary point, i.e., the Euler–Lagrange equation. To ensure that the size effect exhibited in the simulations are originated from the micropolar effect, we adopt the crack surface density functional originally proposed by Wu and Nguyen [6] and Geelen et al. [18] to eliminate the sensitivity of the regularization length scale for the phase field fracture in Boltzmann continua. Our 1D analysis in Section 3.5 and numerical results in Section 5.1 suggest that this same crack surface density functional may also eliminate the sensitivity of the regularization length scale parameter for the micropolar framework.

3.1. Phase field approximation of cohesive fracture

This study adopts a phase field approach to represent cracks via an implicit function [2,43–45]. Let Γ be the discontinuous surface within a micropolar elastic body $\mathcal{B}$. We approximate the fracture surface area A_Γ as A_{Γ_d}, which is the volume integration of crack surface density $\Gamma_d (d, \nabla d)$ over $\mathcal{B}$,

$$A_\Gamma \approx A_{\Gamma_d} = \int_{\mathcal{B}} \Gamma_d (d, \nabla d) \, dV, \tag{15}$$

where d is the phase field which varies from 0 in undamaged regions to 1 in completely damaged regions. In this study, we consider the following crack surface density functional, which is originally used to introduce elliptic regularization of the Mumford–Shah functional for image segmentation [46], i.e.,

$$\Gamma_d (d, \nabla d) = \frac{1}{c_0}\left[\frac{1}{l_c}w(d) + l_c (\nabla d \cdot \nabla d)\right] \; ; \; c_0 = 4\int_0^1 \sqrt{w(s)}\, ds, \tag{16}$$

where l_c is the regularization length scale that governs the size of the diffusive crack zone, $c_0 > 0$ is a normalization constant, and $w(d)$ is one of the function that controls the shape of the regularized profile of the phase field [47–49]. $\Gamma-$convergence requires that the sharp cracks can be recovered by reducing the length scale parameter l_c to zero such that [6,45],

$$A_\Gamma = \lim_{l_c \to 0} A_{\Gamma_d}. \tag{17}$$

The local dissipation function $w(d)$ should be a monotonically increasing function of d, and we distinguish between the following two choices for this function:

$$w(d) = \begin{cases} d^2 \\ d \end{cases}. \tag{18}$$

The quadratic local dissipation $w(d) = d^2$ is the most widely used approach in simulating brittle fracture, and has become the standard in the phase field approximation [2,5,8,21,43,44,50–54]. The major disadvantage of the quadratic local dissipation is that the damage evolution initiates as soon as the load is applied so that there is no pure elastic response. However, the linear model $w(d) = d$, combined with suitable degradation functions, describes the cohesive fracture that possesses a threshold energy that is independent of the regularization length l_c [18,48,55,56]. Also, in this case, the material is characterized by an elastic phase until the stored energy density reaches the threshold value. Since this study aims to decouple the regularization length l_c for large-scale simulations, we adopt the linear dissipation function to take advantage of the aforementioned characteristics. The expression for the crack surface energy density in Eq. (16) then becomes:

$$\Gamma_d\left(d, \nabla d\right) = \frac{3}{8l_c}d + \frac{3l_c}{8}\left(\nabla d \cdot \nabla d\right). \tag{19}$$

3.2. Free energy functional

It should be noted that the crack propagation within a body $\mathcal{B}$ corresponds to the creation of new free surfaces Γ. This implies that the rate of change of the internal energy should be equal to the rate of change of the surface energy that contributes to the crack growth. By assuming that this concept can be applied to the micropolar elastic material as well, the total potential energy Ψ can be defined as follows [18,57]:

$$\Psi = \int_{\mathcal{B}} \psi_e(\bar{\boldsymbol{\varepsilon}}, \bar{\boldsymbol{\kappa}})\, dV + \int_{\Gamma} \mathcal{G}_c\, d\Gamma, \tag{20}$$

where $\mathcal{G}_c$ is critical energy release rate that quantifies the resistance to cracking. Then, revisiting Eqs. (8) and (15), we approximate the functional by

$$\Psi \approx \int_{\mathcal{B}} \psi\, dV, \tag{21}$$

with

$$\psi = \underbrace{g_B(d)\psi_e^{B+}(\bar{\boldsymbol{\varepsilon}}^{\text{sym}}) + g_C(d)\psi_e^C(\bar{\boldsymbol{\varepsilon}}^{\text{skew}}) + g_R(d)\psi_e^R(\bar{\boldsymbol{\kappa}}) + \psi_e^{B-}(\bar{\boldsymbol{\varepsilon}}^{\text{sym}})}_{:=\psi_{\text{bulk}}(\bar{\boldsymbol{\varepsilon}}^{\text{sym}}, \bar{\boldsymbol{\varepsilon}}^{\text{skew}}, \bar{\boldsymbol{\kappa}}, d)} + \mathcal{G}_c\Gamma_d\left(d, \nabla d\right), \tag{22}$$

where $\psi_{\text{bulk}}(\bar{\boldsymbol{\varepsilon}}^{\text{sym}}, \bar{\boldsymbol{\varepsilon}}^{\text{skew}}, \bar{\boldsymbol{\kappa}}, d)$ is the degrading elastic bulk energy, and $g_i(d)$ are the stiffness degradation functions for the corresponding fictitious undamaged energy density parts ψ_e^i ($i = B, C, R$). Here, notice that we decompose $\psi_e^B(\bar{\boldsymbol{\varepsilon}}^{\text{sym}})$ into a positive and negative parts, and degrade only the positive part in order to avoid crack propagation under compression, i.e.,

$$\psi_e^B = \psi_e^{B+} + \psi_e^{B-}. \tag{23}$$

In this study, we adopt the spectral decomposition scheme of Miehe et al. [43], so that each part can be written as:

$$\psi_e^{B\pm} = \frac{1}{2}\left[\lambda\left\langle\bar{\boldsymbol{\varepsilon}}^{\text{sym}} : \boldsymbol{I}\right\rangle_{\pm}^2 + (2\mu + \kappa)\,\bar{\boldsymbol{\varepsilon}}_{\pm}^{\text{sym}} : \bar{\boldsymbol{\varepsilon}}_{\pm}^{\text{sym}}\right] \; ; \; \bar{\boldsymbol{\varepsilon}}_{\pm}^{\text{sym}} = \sum_{a=1}^{3}\left\langle\bar{\varepsilon}_a^{\text{sym}}\right\rangle_{\pm}(\boldsymbol{n}_a \otimes \boldsymbol{n}_a), \tag{24}$$

where $\langle\bullet\rangle_{\pm} = (\bullet \pm |\bullet|)\,/2$ is the Macaulay bracket operator, $\bar{\varepsilon}_a^{\text{sym}}$ is the principal Boltzmann strains, and $\boldsymbol{n}_a$ are the corresponding principal directions.

In order to investigate the effects of each energy density part, one may assume that the partitioned strain energy densities can either be degraded ($i \in \mathfrak{D}$) or remain completely undamaged ($i \in \mathfrak{U}$), i.e.,

$$g_i(d) = \begin{cases} g(d) & \text{if } i \in \mathfrak{D} \\ 1 & \text{if } i \in \mathfrak{U} \end{cases} \; ; \; \mathfrak{D} \cup \mathfrak{U} = \{B, C, R\} \; ; \; \mathfrak{D} \cap \mathfrak{U} = \varnothing. \tag{25}$$

Here, $g(d)$ is a monotonically decreasing function that satisfies the following conditions [58]:

$$g(0) = 1 \; ; \; g(1) = 0 \; ; \; g'(d) \leq 0 \text{ for } d \in [0, 1], \tag{26}$$

where the superposed prime denotes derivative with respect to d. Explicit form of this function is provided in Section 3.4. Notice that this general approach can be tailored to many different situations. For example, one may only degrade the pure Boltzmann part of the strain energy, i.e., $\mathfrak{D} = \{B\}$, $\mathfrak{U} = \{C, R\}$:

$$\psi_{\text{bulk}}(\bar{\boldsymbol{\varepsilon}}^{\text{sym}}, \bar{\boldsymbol{\varepsilon}}^{\text{skew}}, \bar{\boldsymbol{\kappa}}, d) = g(d)\psi_e^{B+}(\bar{\boldsymbol{\varepsilon}}^{\text{sym}}) + \psi_e^C(\bar{\boldsymbol{\varepsilon}}^{\text{skew}}) + \psi_e^R(\bar{\boldsymbol{\kappa}}) + \psi_e^{B-}(\bar{\boldsymbol{\varepsilon}}^{\text{sym}}), \tag{27}$$

or degrade the entire strain energy density, i.e., $\mathfrak{D} = \{B, C, R\}$, $\mathfrak{U} = \varnothing$:

$$\psi_{\text{bulk}}(\bar{\boldsymbol{\varepsilon}}^{\text{sym}}, \bar{\boldsymbol{\varepsilon}}^{\text{skew}}, \bar{\boldsymbol{\kappa}}, d) = g(d)\left[\psi_e^{B+}(\bar{\boldsymbol{\varepsilon}}^{\text{sym}}) + \psi_e^C(\bar{\boldsymbol{\varepsilon}}^{\text{skew}}) + \psi_e^R(\bar{\boldsymbol{\kappa}})\right] + \psi_e^{B-}(\bar{\boldsymbol{\varepsilon}}^{\text{sym}}). \tag{28}$$

3.3. Derivation of Euler–Lagrange equations via variational principle

Let $\mathbb{V}$ denote an appropriate function space. Then, based on the fundamental lemma of calculus of variations, the necessary condition for the energy functional $\Psi : \mathbb{V} \to \mathbb{R}$ in Eq. (21) to have a local extremum at a point $\boldsymbol{\chi}_0 \in \mathbb{V}$ is that,

$$\frac{\delta\psi}{\delta\boldsymbol{\chi}}(\boldsymbol{\chi}_0) = \mathbf{0}, \tag{29}$$

where ψ is the energy density that is previously defined in Eq. (22), $\boldsymbol{\chi} := \{\boldsymbol{u}, \boldsymbol{\theta}, d\}$ indicates the field variables, and $\delta(\bullet)/\delta\boldsymbol{\chi}$ denotes the functional derivative with respect to $\boldsymbol{\chi}$. Notice that Eq. (29) is the so-called Euler–Lagrange equations, which yield the governing partial differential equations to be solved.

The linear momentum balance equation can be recovered by seeking the stationary point where the functional derivative of ψ with respect to $\boldsymbol{u}$ vanishes. By assuming no body forces and by only considering the single derivative, we have,

$$\frac{\delta\psi}{\delta\boldsymbol{u}} = \frac{\partial\psi}{\partial\boldsymbol{u}} - \nabla \cdot \frac{\partial\psi}{\partial\nabla\boldsymbol{u}} = \mathbf{0}. \tag{30}$$

By revisiting Eq. (22), we get:

$$\frac{\partial\psi}{\partial\boldsymbol{u}} = \mathbf{0}, \tag{31}$$

and by Eq. (12),

$$\nabla \cdot \frac{\partial\psi}{\partial\nabla\boldsymbol{u}} = \nabla \cdot \left[g_B(d)\frac{\partial\psi_e^B}{\partial\nabla\boldsymbol{u}} + g_C(d)\frac{\partial\psi_e^C}{\partial\nabla\boldsymbol{u}}\right] = \nabla \cdot \left[g_B(d)\bar{\boldsymbol{\sigma}}^B + g_C(d)\bar{\boldsymbol{\sigma}}^C\right], \tag{32}$$

since the decomposition of the micropolar strain in Eq. (3) yields the following:

$$\frac{\partial\psi_e^B}{\partial\nabla\boldsymbol{u}} = \frac{\partial\psi_e^B}{\partial\bar{\boldsymbol{\varepsilon}}^{\text{sym}}} : \frac{\partial\bar{\boldsymbol{\varepsilon}}^{\text{sym}}}{\partial\nabla\boldsymbol{u}} = \frac{\partial\psi_e^B}{\partial\bar{\boldsymbol{\varepsilon}}^{\text{sym}}} : \frac{1}{2}\left(\mathbb{I} + \bar{\mathbb{I}}\right) = \frac{\partial\psi_e^B}{\partial\bar{\boldsymbol{\varepsilon}}^{\text{sym}}} = \bar{\boldsymbol{\sigma}}^B, \tag{33}$$

$$\frac{\partial\psi_e^C}{\partial\nabla\boldsymbol{u}} = \frac{\partial\psi_e^C}{\partial\bar{\boldsymbol{\varepsilon}}^{\text{skew}}} : \frac{\partial\bar{\boldsymbol{\varepsilon}}^{\text{skew}}}{\partial\nabla\boldsymbol{u}} = \frac{\partial\psi_e^C}{\partial\bar{\boldsymbol{\varepsilon}}^{\text{skew}}} : \frac{1}{2}\left(\bar{\mathbb{I}} - \mathbb{I}\right) = \frac{\partial\psi_e^C}{\partial\bar{\boldsymbol{\varepsilon}}^{\text{skew}}} = \bar{\boldsymbol{\sigma}}^C. \tag{34}$$

Similarly, assuming no body couples, the balance of angular momentum can be obtained by searching the local extremum where the functional derivative of ψ with respect to the micro-rotation $\boldsymbol{\theta}$ vanishes, i.e.,

$$\frac{\delta\psi}{\delta\boldsymbol{\theta}} = \frac{\partial\psi}{\partial\boldsymbol{\theta}} - \nabla \cdot \frac{\partial\psi}{\partial\nabla\boldsymbol{\theta}} = \mathbf{0}. \tag{35}$$

The partial derivative of ψ with respect to $\boldsymbol{\theta}$ is:

$$\frac{\partial\psi}{\partial\boldsymbol{\theta}} = g_C(d)\frac{\partial\psi_e^C}{\partial\boldsymbol{\theta}} = g_C(d)\frac{\partial\psi_e^C}{\partial\bar{\boldsymbol{\varepsilon}}^{\text{skew}}} : \frac{\partial\bar{\boldsymbol{\varepsilon}}^{\text{skew}}}{\partial\boldsymbol{\theta}} = -\overset{3}{\boldsymbol{E}} : \left[g_C(d)\bar{\boldsymbol{\sigma}}^C\right]. \tag{36}$$

By Eq. (13), the partial derivative of ψ with respect to $\nabla\boldsymbol{\theta}$ becomes:

$$\nabla \cdot \frac{\partial\psi}{\partial\nabla\boldsymbol{\theta}} = \nabla \cdot \left[g_R(d)\frac{\partial\psi_e^R}{\partial\bar{\boldsymbol{\kappa}}}\right] = \nabla \cdot \left[g_R(d)\bar{\boldsymbol{m}}^R\right]. \tag{37}$$

The damage evolution equation (i.e., functional derivative of ψ with respect to the phase field d) can also be recovered as follows:

$$\frac{\delta\psi}{\delta d} = \frac{\partial\psi}{\partial d} - \nabla \cdot \frac{\partial\psi}{\partial\nabla d} = 0, \tag{38}$$

where, by revisiting Eq. (19),

$$\frac{\partial \psi}{\partial d} = g'(d) \left[\sum_{i \in \mathfrak{D}} \psi_e^i \right] + \frac{3\mathcal{G}_c}{8l_c},\tag{39}$$

and

$$\nabla \cdot \frac{\partial \psi}{\partial \nabla d} = \nabla \cdot \left(\frac{3\mathcal{G}_c l_c}{4} \nabla d \right).\tag{40}$$

Finally, collecting the terms from Eqs. (30)–(40), we obtain the following coupled system of partial differential equations to be solved:

$$\nabla \cdot \left[g_B(d)\bar{\boldsymbol{\sigma}}^B + g_C(d)\bar{\boldsymbol{\sigma}}^C \right] = \mathbf{0} \qquad \text{balance of linear momentum,}\tag{41}$$

$$\nabla \cdot \left[g_R(d)\bar{\boldsymbol{m}}^R \right] + \overset{3}{\boldsymbol{E}} : \left[g_C(d)\bar{\boldsymbol{\sigma}}^C \right] = \mathbf{0} \qquad \text{balance of angular momentum,}\tag{42}$$

$$g'(d)\mathcal{F} + \frac{3}{8} \left(1 - 2l_c^2 \nabla^2 d \right) = 0 \qquad \text{nondimensionalized damage evolution equation,}\tag{43}$$

where $\nabla^2(\bullet) = \nabla \cdot \nabla(\bullet)$ is the Laplacian operator, and $\mathcal{F}$ is the degrading nondimensionalized strain energy density:

$$\mathcal{F} = \frac{\displaystyle\sum_{i \in \mathfrak{D}} \psi_e^i}{\mathcal{G}_c/l_c}.\tag{44}$$

3.4. Crack irreversibility and degradation function

As far as $\mathfrak{D} \neq \varnothing$, we prevent crack healing by following the treatment used in [8,21,59] which ensures the irreversibility constraint by enforcing the driving force to be non-negative. Although the stored energy density is split into three different parts, we simply introduce one distinct history function or driving force $\mathcal{H}$ which is the pseudo-temporal maximum of the degrading nondimensionalized energy density. Inserting our definition into Eq. (43) gives:

$$g'(d)\mathcal{H} + \frac{3}{8} \left(1 - 2l_c^2 \nabla^2 d \right) = 0.\tag{45}$$

Revisiting Section 3.1, the term cohesive denotes that the model should possess a threshold for the loading, where damage does not develop below this value. Therefore, we particularly restrict the crack growth to initiate above a threshold energy density ψ_{crit} by using the following history function, in order to approximate the cohesive response:

$$\mathcal{H} = \max_{\tau \in [0,t]} \left\{ \mathcal{F}_{\text{crit}} + \mathcal{F}_{\text{crit}} \left\langle \frac{\mathcal{F}}{\mathcal{F}_{\text{crit}}} - 1 \right\rangle_+ \right\} \quad ; \quad \mathcal{F}_{\text{crit}} = \frac{\psi_{\text{crit}}}{\mathcal{G}_c/l_c},\tag{46}$$

where $\mathcal{F}_{\text{crit}}$ is the nondimensionalized threshold energy. Note that Eq. (45) is the field equation that is actually solved for the phase field in this study.

We complete our formulation by specifying the degradation function $g(d)$. This study adopts a quasi-quadratic degradation function [18,55,60], which is a rational function of the phase field d. The quasi-quadratic degradation function has an associated upper bound on the regularization length l_c, and is defined as:

$$g(d) = \frac{(1-d)^2}{(1-d)^2 + md(1+pd)} \quad ; \quad l_c \leq \frac{3\mathcal{G}_c}{8(p+2)\psi_{\text{crit}}},\tag{47}$$

where $m \geq 1$ is constant, and $p \geq 1$ is a shape parameter that controls the peak stress and the fracture responses.

Recall that this study restricts the damage evolution to initiate above a threshold energy. In other words, below the threshold (i.e., $\mathcal{F}/\mathcal{F}_{\text{crit}} \leq 1$), the driving force and the phase field should satisfy $\mathcal{H} = \mathcal{F}_{\text{crit}}$ and $d = 0$, respectively. In this case, the damage evolution equation [Eq. (45)] becomes:

$$g'(0)\mathcal{F}_{\text{crit}} + \frac{3}{8} = 0.\tag{48}$$

Since the degradation function [Eq. (47)] yields $g'(0) = -m$, we require

$$m = \frac{3}{8\mathcal{F}_{\text{crit}}},$$ (49)

in order to trivially satisfy Eq. (48). Again, the most common choice for the degradation function would be a simple quadratic function, i.e., $g(d) = (1-d)^2$. A phase field model that adopts the quadratic degradation function requires a particular critical energy ψ_{crit} that depends on l_c to satisfy Eq. (48). However, by using the quasi-quadratic degradation function in Eq. (47) with Eq. (49), it is noted that the threshold energy density ψ_{crit} is no longer dependent on l_c, since the degradation function itself is designed to automatically satisfy Eq. (48). It reveals that the elastic response (i.e., if stored energy is below the threshold) is regularization length independent. The regularization length insensitivity of the model, for the case where the stored energy exceeds the threshold, will be discussed in Section 3.5.

3.5. One-dimensional analysis on phase field regularization length sensitivity

In order to gain insights on the regularization length insensitive response, we consider a similar 1D boundary value problem previously used in [6,18] for length scale analysis. Our major departure is that the material is now an analog to the micropolar material where a length scale dependent state variable (which replaces the micro-rotation due to the low-dimensional kinematics) is introduced to replicate the size effect of the elasticity response. Consider a one-dimensional bar $x \in [-L, L]$ subjected to a tensile loading on both ends. We assume that the length $2L$ is sufficiently long enough so that the any possible boundary effects can be neglected. We define the strain measures as $\bar{\varepsilon} = du/dx$, and $\bar{\kappa} = l_e(d\theta/dx)$, where l_e is the length scale. Our goal here is to check whether the size-dependent responses in the damaged zone are sensitive to the regularization length scale for the phase field l_c. Note that this formulation does yield size-dependent responses in both elastic and damage zones, but the kinematics in 1D does not permit rotation. Hence, θ and $\bar{\kappa}$ no longer indicate micro-rotation and micro-curvature respectively. Thus, analogous to Eq. (8), we introduce a 1D size-dependent model of which the strain energy density takes a quadratic form as:

$$\psi_e = \frac{1}{2}C_B \left(\frac{du}{dx}\right)^2 + \frac{1}{2}C_C \left(\frac{du}{dx} - l_e\frac{d\theta}{dx}\right)^2 + \frac{1}{2}C_R l_e^2 \left(\frac{d\theta}{dx}\right)^2,$$ (50)

where $C_B > 0$, $C_C > 0$ and $C_R > 0$ are the material parameters. Notice that (1) this stored energy functional does not admit non-trivial zero-energy mode provided that $C_B + C_C > 0$ and $C_R > 0$ and (2) if the length scale l_e vanishes, Eq. (50) reduces to an energy functional for the classical Boltzmann continuum. In this setting, the stress measures can be obtained as,

$$\bar{\sigma} = \frac{\partial \psi_e}{\partial \bar{\varepsilon}} = C_B\bar{\varepsilon} + C_C (\bar{\varepsilon} - \bar{\kappa}),$$ (51)

$$\bar{m} = \frac{\partial \psi_e}{\partial \bar{\kappa}} = C_R\bar{\kappa} - C_C (\bar{\varepsilon} - \bar{\kappa}),$$ (52)

where both $\bar{\sigma}$ and $\bar{m}$ are l_e-dependent. Assuming all energy density parts can be degraded, the Lagrangian for the damaged state where $\psi_e > \psi_{\text{crit}}$ then becomes:

$$\psi = g(d)\psi_e + \frac{3\mathcal{G}_c}{8l_c}\left[d + l_c^2\left(\frac{dd}{dx}\right)^2\right],$$ (53)

where $g(d)$ is previously defined in Eq. (47). The first variation of Eq. (53) yields the following set of Euler–Lagrange equations:

$$\frac{d}{dx}[g(d)\bar{\sigma}] = 0,$$ (54)

$$\frac{d}{dx}[g(d)\bar{m}] = 0,$$ (55)

$$g'(d)\frac{\psi_e}{\mathcal{G}_c/l_c} + \frac{3}{8}\left(1 - 2l_c^2\frac{d^2d}{dx^2}\right) = 0,$$ (56)

where Eqs. (54) and (55) are the balance equations, and Eq. (56) is the nondimensionalized damage evolution equation. Following [18], we apply a specific amount of $\bar{\sigma}$ at both ends while the boundaries remain $\bar{m}$-free, such that Eqs. (54) and (55) yield:

$$g(d)\bar{\sigma} = \bar{\sigma}_0 \; ; \; g(d)\bar{m} = 0, \tag{57}$$

where $\bar{\sigma}_0$ is the responding stress on the boundary ($x = \pm L$). By the constitutive relationships in Eqs. (51)–(52), we can now express the strain measures $\bar{\varepsilon}$ and $\bar{\kappa}$ as,

$$\bar{\varepsilon} = \frac{C_C - C_R}{C_B(C_C - C_R) - C_C C_R} \frac{\bar{\sigma}_0}{g(d)} \; ; \; \bar{\kappa} = \frac{C_C}{C_B(C_C - C_R) - C_C C_R} \frac{\bar{\sigma}_0}{g(d)}. \tag{58}$$

Thus, the energy density functional in Eq. (50) can be rewritten as:

$$\psi_e = \frac{\bar{\sigma}_0^2}{C^* g(d)^2} \; ; \; C^* = \frac{2\,[C_B(C_C - C_R) - C_C C_R]^2}{C_B(C_C - C_R)^2 + C_C C_R(C_C + C_R)}. \tag{59}$$

Substituting Eqs. (57) and (59) into Eq. (56), we get,

$$g'(d) \left[\frac{1}{\mathcal{G}_c/l_c} \frac{\bar{\sigma}_0^2}{C^* g(d)^2} \right] + \frac{3}{8} \left(1 - 2l_c^2 \frac{d^2 d}{dx^2} \right) = 0. \tag{60}$$

By multiplying Eq. (60) with dd/dx, we can obtain the following differential equation:

$$\frac{d}{dx} \left\{ \frac{3}{8} \left[d - l_c^2 \left(\frac{dd}{dx} \right)^2 \right] - \frac{1}{\mathcal{G}_c/l_c} \frac{\bar{\sigma}_0^2}{2C^* g(d)} \right\} = 0. \tag{61}$$

Following [6,18], we focus on the damaged zone $[-l_z, l_z]$ with $l_z \ll L$, where the outer edge of the zone is related to the parameter d^*, the maximum value of the damage across the bar (i.e., $d^* = 1$ if the bar is fully broken). Then, by symmetry, at $x = 0$ we have:

$$d(d^*, 0) = d^* \; ; \; \frac{dd}{dx}(d^*, 0) = 0, \tag{62}$$

while the boundary conditions at the outer edge $x = l_z$ are given by,

$$d(d^*, l_z) = 0 \; ; \; \frac{dd}{dx}(d^*, l_z) = 0. \tag{63}$$

By introducing the parameter d^*, notice that our goal is to find the expression for the responding stress $\bar{\sigma}_0$ as a function of the maximum damage d^*, or vice versa. Integration of Eq. (61), using boundary conditions in Eq. (63) admits the following:

$$\frac{3}{8} \left[d - l_c^2 \left(\frac{dd}{dx} \right)^2 \right] = \frac{1}{\mathcal{G}_c/l_c} \frac{\bar{\sigma}_0^2}{2C^*} \left(g(d)^{-1} - 1 \right). \tag{64}$$

Applying the symmetry conditions [Eq. (62)], Eq. (64) becomes:

$$\frac{\bar{\sigma}_0^2}{2C^*} = \frac{3\mathcal{G}_c}{8l_c} \frac{d^*}{g(d^*)^{-1} - 1}. \tag{65}$$

Substituting the expression of the degradation function in Eq. (47) and the expression for the degradation parameter m in Eq. (49), we finally get:

$$\bar{\sigma}_0 = \sqrt{2C^* \psi_{\text{crit}} \frac{(1 - d^*)^2}{1 + pd^*}}. \tag{66}$$

Observe that the resultant stress $\bar{\sigma}_0$ can be expressed in terms of d^* but independent of the phase field regularization length l_c. Eq. (66) highlights that the proposed model is capable of replicating the global response insensitive to regularization length l_c for the phase field, while preserving the size effect introduced by the micropolar elasticity. This result is important, as this insensitivity to l_c enables us to simulate cohesive fracture in large spatial domain composed of micropolar materials. Extending this analysis for 2D and 3D cases is out of the scope of this study but will be considered in the future.

Remark 1. Previous works on phase field and gradient damage models for cohesive fracture in Cauchy continuum, such as [55,61,62], have established a connection between the cohesive zone models and the phase field and gradient damage models that represent cracks via implicit function. In principle, it is possible that similar connection can be established between the micropolar phase field model presented in this paper and the established micropolar cohesive zone models such as [63–65]. Such an endeavor is obviously out of the scope of this study due to the extensive length, but will be considered in future studies.

4. Finite element implementation

In this section, we describe the finite element discretization, followed by the solution strategy to solve the system of nonlinear equation incrementally. Starting from the strong form, we follow the standard procedure to recover the variational form while employing the Taylor–Hood finite element space for the displacement and micro-rotation fields, and standard linear interpolation for the phase field. This finite element space is chosen to match the design of the operator-split algorithm. The displacement and micro-rotation are updated in a monolithic manner, where we use Taylor–Hood element such that the displacement field is interpolated by quadratic polynomials and the micro-rotation is interpolated by linear polynomials. Meanwhile, the phase field is also interpolated by linear function to ensure the efficiency of the staggered solver that updates the phase field while holding the displacement and micro-rotation fixed. The operator-split solution scheme (i.e., staggered scheme) that successively updates the field variables is described in Section 4.2.

4.1. Galerkin form

We derive the weak form and introduce the finite dimensional space to introduce the numerical scheme for the boundary value problems described in Eqs. (41)–(42) and Eq. (45). We consider a micropolar elastic domain $\mathcal{B}$ with boundary $\partial\mathcal{B}$ composed of Dirichlet boundaries (displacement $\partial\mathcal{B}_u$ and micro-rotation $\partial\mathcal{B}_\theta$) and Neumann boundaries (traction $\partial\mathcal{B}_{t_\sigma}$ and moment $\partial\mathcal{B}_{t_m}$) satisfying,

$$\partial\mathcal{B} = \overline{\partial\mathcal{B}_u \cup \partial\mathcal{B}_{t_\sigma}} = \overline{\partial\mathcal{B}_\theta \cup \partial\mathcal{B}_{t_m}} \ ; \ \varnothing = \partial\mathcal{B}_u \cap \partial\mathcal{B}_{t_\sigma} = \partial\mathcal{B}_\theta \cap \partial\mathcal{B}_{t_m}. \tag{67}$$

The prescribed boundary conditions can be specified as:

$$\begin{cases} \boldsymbol{u} = \hat{\boldsymbol{u}} & \text{on } \partial\mathcal{B}_u, \\ \boldsymbol{\theta} = \hat{\boldsymbol{\theta}} & \text{on } \partial\mathcal{B}_\theta, \\ \left[g_B(d)\bar{\boldsymbol{\sigma}}^B + g_C(d)\bar{\boldsymbol{\sigma}}^C \right]^{\mathrm{T}} \cdot \boldsymbol{n} = \hat{\boldsymbol{t}}_\sigma & \text{on } \partial\mathcal{B}_{t_\sigma}, \\ \left[g_R(d)\bar{\boldsymbol{m}}^R \right]^{\mathrm{T}} \cdot \boldsymbol{n} = \hat{\boldsymbol{t}}_m & \text{on } \partial\mathcal{B}_{t_m}, \\ \nabla d \cdot \boldsymbol{n} = 0 & \text{on } \partial\mathcal{B}, \end{cases} \tag{68}$$

where $\boldsymbol{n}$ is the outward-oriented unit normal on the boundary surface $\partial\mathcal{B}$; $\hat{\boldsymbol{u}}, \hat{\boldsymbol{\theta}}, \hat{\boldsymbol{t}}_\sigma, \hat{\boldsymbol{t}}_m$ are the prescribed displacement, micro-rotation, traction and moment, respectively; and the degradation functions $g_i(d)$ ($i = B, C, R$) are previously defined in Eq. (25). For the model closure, the initial conditions are imposed as,

$$\boldsymbol{u} = \boldsymbol{u}_0 \ ; \ \boldsymbol{\theta} = \boldsymbol{\theta}_0, \tag{69}$$

at $t = 0$.

We define the trial spaces V_u, V_θ, and V_d for the solution variables:

$$V_u = \left\{ \boldsymbol{u} : \mathcal{B} \to \mathbb{R}^3 \mid \boldsymbol{u} \in [H^1(\mathcal{B})]^3, \ \boldsymbol{u}|_{\partial\mathcal{B}_u} = \hat{\boldsymbol{u}} \right\}, \tag{70}$$

$$V_\theta = \left\{ \boldsymbol{\theta} : \mathcal{B} \to \mathbb{R}^3 \mid \boldsymbol{\theta} \in [H^1(\mathcal{B})]^3, \ \boldsymbol{\theta}|_{\partial\mathcal{B}_\theta} = \hat{\boldsymbol{\theta}} \right\}, \tag{71}$$

$$V_d = \left\{ d : \mathcal{B} \to \mathbb{R} \mid d \in H^1(\mathcal{B}) \right\}, \tag{72}$$

where H^1 denotes the Sobolev space of order 1. Notice that this study adopts Taylor–Hood finite element (i.e., quadratic interpolation for displacement and linear for micro-rotation) following [66], which showed that the cohesive fracture model exhibits stress oscillation when equal order polynomials are used for the solution field, while the discretization with high order interpolation function for the displacement and first order functions for the

auxiliary field and the phase field seems to eliminate this oscillation. Similarly, the corresponding admissible spaces for Eqs. (70)–(72) with homogeneous boundary conditions are defined as,

$$V_\eta = \left\{ \boldsymbol{\eta} : \mathcal{B} \to \mathbb{R}^3 \mid \boldsymbol{\eta} \in [H^1(\mathcal{B})]^3, \ \boldsymbol{\eta}|_{\partial \mathcal{B}_u} = \mathbf{0} \right\}, \tag{73}$$

$$V_\xi = \left\{ \boldsymbol{\xi} : \mathcal{B} \to \mathbb{R}^3 \mid \boldsymbol{\xi} \in [H^1(\mathcal{B})]^3, \ \boldsymbol{\xi}|_{\partial \mathcal{B}_\theta} = \mathbf{0} \right\}, \tag{74}$$

$$V_\zeta = \left\{ \zeta : \mathcal{B} \to \mathbb{R} \mid \zeta \in H^1(\mathcal{B}) \right\}. \tag{75}$$

Applying the standard weighted residual procedure, the weak statements for Eqs. (41)–(42) and Eq. (45) are to: find $\{\boldsymbol{u}, \boldsymbol{\theta}, d\} \in V_u \times V_\theta \times V_d$ such that for all $\{\boldsymbol{\eta}, \boldsymbol{\xi}, \zeta\} \in V_\eta \times V_\xi \times V_\zeta$,

$$G_u(\boldsymbol{u}, \boldsymbol{\theta}, d, \boldsymbol{\eta}) = G_\theta(\boldsymbol{u}, \boldsymbol{\theta}, d, \boldsymbol{\xi}) = G_d(\boldsymbol{u}, \boldsymbol{\theta}, d, \zeta) = 0. \tag{76}$$

Here, $G_u \to \mathbb{R}$ is the weak statement of the balance of linear momentum:

$$G_u = \int_{\mathcal{B}} \nabla \boldsymbol{\eta} : \left[g_B(d) \bar{\boldsymbol{\sigma}}^B + g_C(d) \bar{\boldsymbol{\sigma}}^C \right] dV - \int_{\partial \mathcal{B}_{t_\sigma}} \boldsymbol{\eta} \cdot \hat{\boldsymbol{t}}_\sigma \, dA = 0, \tag{77}$$

$G_\theta \to \mathbb{R}$ is the weak statement of the balance of angular momentum:

$$G_\theta = \int_{\mathcal{B}} \nabla \boldsymbol{\xi} : g_R(d) \bar{\boldsymbol{m}}^R \, dV - \int_{\mathcal{B}} \boldsymbol{\xi} \cdot \overset{3}{\boldsymbol{E}} : \left[g_C(d) \bar{\boldsymbol{\sigma}}^C \right] dV - \int_{\partial \mathcal{B}_{t_m}} \boldsymbol{\xi} \cdot \hat{\boldsymbol{t}}_m \, dA = 0, \tag{78}$$

and $G_d \to \mathbb{R}$ is the weak statement of the damage evolution equation:

$$G_d = \int_{\mathcal{B}} \zeta \cdot g'(d) \mathcal{H} \, dV + \frac{3}{8} \left[\int_{\mathcal{B}} \zeta + 2 l_c^2 \, (\nabla \zeta \cdot \nabla d) \, dV \right] = 0, \tag{79}$$

where $\mathcal{H}$ and $g(d)$ are previously defined in Eqs. (46) and (47), respectively.

4.2. Operator-split solution scheme

As previous studies on the phase field model showed that the operator splitting (i.e., staggered scheme) may potentially be more robust compared to the monolithic approach [43,67,68], this study adopts the solution procedure based on the operator-split scheme to successively update three field variables $\{\boldsymbol{u}, \boldsymbol{\theta}, d\}$. In this operator-split setting, the damage field is updated first while the displacement and micro-rotation fields are held fixed. A new damage field d_{n+1} is obtained iteratively once the algorithm converges within a predefined tolerance. Then, the linear solver holds the damage field fixed and advances the displacement and the micro-rotation fields $\{\boldsymbol{u}_{n+1}, \boldsymbol{\theta}_{n+1}\}$. The schematic of the solution strategy can be summarized as follows:

$$\begin{bmatrix} \boldsymbol{u}_n \\ \boldsymbol{\theta}_n \\ d_n \end{bmatrix} \xrightarrow{\mathcal{R}(d)=0} \underbrace{\begin{bmatrix} \boldsymbol{u}_n \\ \boldsymbol{\theta}_n \\ d_{n+1} \end{bmatrix}}_{\text{Iterative solver}} \overset{\overbrace{\qquad\qquad}^{\text{Linear solver}}}{\xrightarrow{\mathcal{R}(\boldsymbol{u},\boldsymbol{\theta})=\mathbf{0}}} \begin{bmatrix} \boldsymbol{u}_{n+1} \\ \boldsymbol{\theta}_{n+1} \\ d_{n+1} \end{bmatrix}, \tag{80}$$

where $\mathcal{R}(\boldsymbol{u}, \boldsymbol{\theta})$ and $\mathcal{R}(d)$ are the residuals that are consistent with Eqs. (77)–(79):

$$\mathcal{R}(\boldsymbol{u}, \boldsymbol{\theta}) : \begin{cases} \int_{\mathcal{B}} \nabla \boldsymbol{\eta} : \left[g_B(d_{n+1}) \bar{\boldsymbol{\sigma}}^B_{n+1} + g_C(d_{n+1}) \bar{\boldsymbol{\sigma}}^C_{n+1} \right] dV - \int_{\partial \mathcal{B}_{t_\sigma}} \boldsymbol{\eta} \cdot \hat{\boldsymbol{t}}_\sigma \big|_{n+1} \, dA, \\ \int_{\mathcal{B}} \nabla \boldsymbol{\xi} : g_R(d_{n+1}) \bar{\boldsymbol{m}}^R_{n+1} \, dV - \int_{\mathcal{B}} \boldsymbol{\xi} \cdot \overset{3}{\boldsymbol{E}} : \left[g_C(d_{n+1}) \bar{\boldsymbol{\sigma}}^C_{n+1} \right] dV - \int_{\partial \mathcal{B}_{t_m}} \boldsymbol{\xi} \cdot \hat{\boldsymbol{t}}_m \big|_{n+1} \, dA \end{cases} \tag{81}$$

$$\mathcal{R}(d) : \left\{ \int_{\mathcal{B}} \zeta \cdot g'(d_{n+1}) \mathcal{H}_n \, dV + \frac{3}{8} \left[\int_{\mathcal{B}} \zeta + 2 l_c^2 \, (\nabla \zeta \cdot \nabla d_{n+1}) \, dV \right] . \tag{82}$$

It should be noticed that one may choose other strategies to solve the same system of equations, however, the exploration of different schemes are out of the scope of this study.

The implementation of the numerical models including the finite element discretization and the operator-split solution scheme rely on the finite element package FEniCS [69–72] with PETSc scientific computation toolkit [73]. The scripts developed for this study are open-sourced (available at https://github.com/hyoungsuksuh/micropolar_ph asefield), in order to aid third-party verification and validation [74].
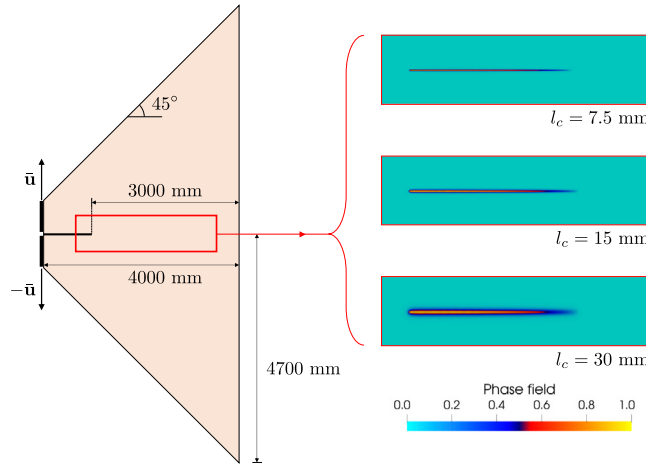
Fig. 2. Schematic of geometry and boundary conditions for a trapezoidal domain and the observed crack patterns at $\bar{u} = 0.325$ mm with different regularization lengths.

5. Numerical examples

This section presents numerical examples to showcase the applicability of the proposed phase field model for damaged micropolar elastic material. For simplicity, we limit our attention to two-dimensional simulations in this section. Based on the 2D setting, the kinematic state of the micropolar elastic body can be described by two in-plane displacements $\boldsymbol{u} = [u_1, u_2]^{\mathrm{T}}$ and one out-of-plane micro-rotation angle θ_3. Since the material elasticity now only depends on bending characteristic length, we now require only four engineering material parameters (e.g., E, ν, N, and l_b).

The first example serves as a verification test that highlights the regularization length insensitive response of the phase field model with quasi-quadratic degradation function in Eq. (47). We then investigate the effect of scale-dependent elasticity on the crack patterns, by simulating asymmetric notched three-point bending tests with different coupling numbers N and single edge notched tests with different characteristic lengths l_b, respectively. Finally, we exhibit the applicability of the proposed energy split scheme by considering different degradation functions on the partitioned energy densities. All the numerical simulations rely on meshes that are sufficiently refined to properly capture the damage field around crack surfaces. Unless specified, we especially adopt the element size of $h^e \approx l_c/10$ around the potential crack propagation trajectory.

5.1. Verification exercise: the trapezoid problem

We first examine a problem proposed by Lorentz et al. [55] that has a trapezoidal-shaped symmetrical domain with an initial notch. Since we prescribe the displacement $\bar{\boldsymbol{u}}$ in order to consider pure Mode I loading, as illustrated in Fig. 2, this specific geometry helps us to avoid crack kinking and to facilitate straight crack propagation. The aforementioned characteristics of the trapezoid problem make it suitable for verifying the regularization length insensitive response of the cohesive phase field model with quasi-quadratic degradation. This example thus performs a parametric study for three different regularization lengths ($l_c = 7.5$, 15, and 30 mm, as depicted in Fig. 2), with two different shape parameters $p = 2.5$ and 10.

The material is assumed to be similar to the concrete studied in [55]. The material parameters for this example are chosen as follows: Young's modulus $E = 30$ GPa, Poisson's ratio $\nu = 0.2$, critical energy release rate $\mathcal{G}_c = 0.1$ N/mm, and threshold energy density $\psi_{\mathrm{crit}} = 0.1$ kJ/m^3. We also set coupling number $N = 0$ and bending characteristic length $l_b = 0$ mm in order to avoid all the micropolar effects, and at the same time damage only the pure Boltzmann part, i.e., $\mathfrak{D} = \{B\}$, $\mathfrak{U} = \{C, R\}$. We prescribe $\Delta \bar{u}_2 = 0.5 \times 10^{-3}$ mm on the left boundaries, while all other boundaries are maintained traction-free during the simulations.

Fig. 3 shows the force–displacement curves for the trapezoid problem, corroborated by other numerical observations [18,55]. The results indicate that the shape parameter p is able to influence the peak force and the

(a) Shape parameter $p = 2.5$.

(b) Shape parameter $p = 10$.
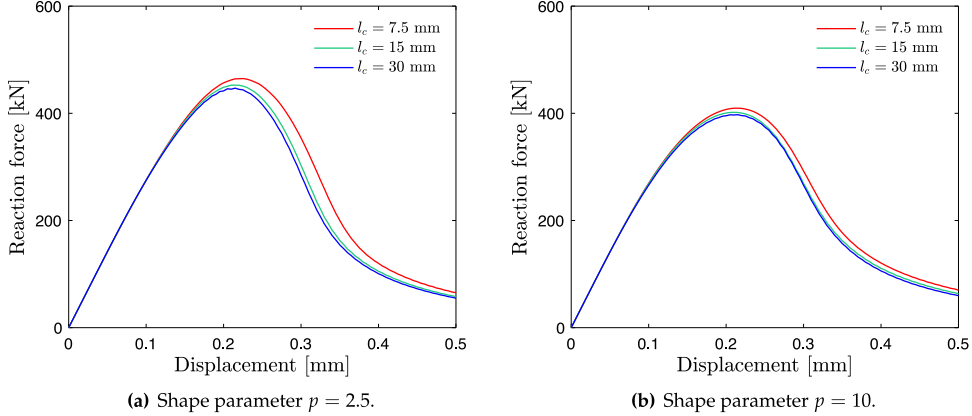
Fig. 3. The force–displacement curves obtained from the trapezoid problem with different regularization lengths: non-polar case.
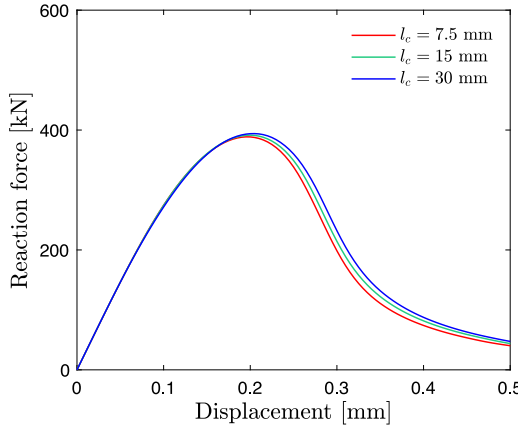


Fig. 4. The force–displacement curve obtained from the trapezoid problem with different regularization lengths: micropolar case, $p = 10$, $l_b = 50$ mm, and $N = 0.5$.

overall global force–displacement responses. In fact, the quasi-quadratic degradation function enables us to not only tailor the threshold for the elastic region by controlling ψ_{crit}, but also tune the peak stress by varying shape parameter p. As pointed out in [18], higher value of p tends to significantly elongate the length of the fracture process zone, such that the stresses in the process zone can effectively be smeared over a large distance. As a result, we can observe that an increasing value of p yields the global force–displacement response where the effect of using different length scale parameters l_c becomes negligible, as previously reported in [6,18,27,55].

We then repeat the same problem with the micropolar material, i.e., the case where $\mathfrak{D} = \{B, C, R\}$, $\mathfrak{U} = \varnothing$. Recall Section 3.5 that the regularization length insensitive response is expected for the micropolar material as well. For this problem, we set coupling number $N = 0.5$, and bending characteristic length $l_b = 50$ mm, while we choose the shape parameter as $p = 10$ which produced regularization length insensitive results in Fig. 3(b). As illustrated in Fig. 4, the force–displacement curve confirms that our choice $p = 10$ yields the regularization length insensitive global response for micropolar material as well. These evidences suggest that a sufficiently high shape parameter p may yield the material responses insensitive to the phase field length scale parameter in both non-polar and micropolar materials.

5.2. Single edge notched tests

We present the results obtained from simulating the classical single-edge notched tests to investigate the size effect of elasticity and energy dissipation during the crack nucleation and propagation. The problem domain is
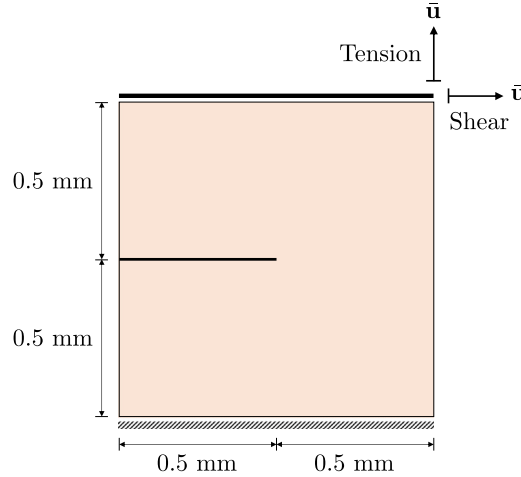
Fig. 5. Schematic of geometry and boundary conditions for the single edge notched tests.
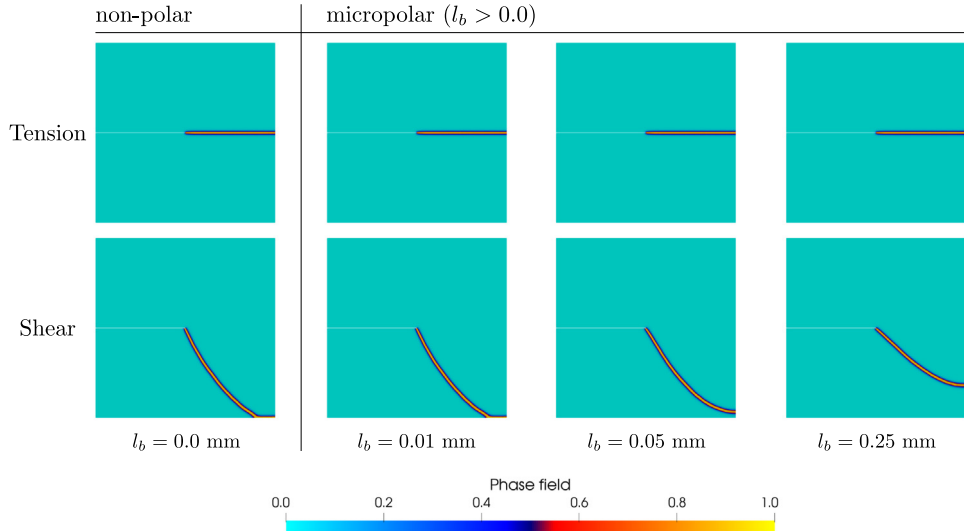
Fig. 6. Fracture patterns for single edge notched tests under different micropolar characteristic length l_b.

a square plate that has an initial horizontal edge crack placed at the middle from the left to the center (Fig. 5). Similar to the previous studies [43,44], we choose material parameters as: $E = 210$ GPa, $\nu = 0.3$, $\mathcal{G}_c = 2.7$ N/mm, $l_c = 0.008$ mm, and $\psi_{\text{crit}} = 10$ MJ/m^3. Numerical experiments are conducted with different bending characteristic lengths: $l_b = 0.0, 0.01, 0.05,$ and 0.25 mm while the coupling number is held fixed as $N = 0.5$. Also, for this problem we damage all the energy density parts, i.e., $\mathfrak{D} = \{B, C, R\}$, $\mathfrak{U} = \varnothing$. As illustrated in Fig. 5, two different types of simulations are conducted with the same specimen: the pure tensile test with prescribed vertical displacement $\Delta \bar{u}_2 = 2.0 \times 10^{-5}$ mm; and the pure shear test with prescribed horizontal displacement $\Delta \bar{u}_1 = 2.0 \times 10^{-5}$ mm. In both cases, the displacements are prescribed along the entire top boundary, while the bottom part of the domain is fixed.

Fig. 6 illustrates the crack trajectories at the completely damaged stages for both tension and shear tests with different the bending characteristic lengths. The results clearly show that pure tensile loading exhibits the same crack pattern regardless of l_b. This result is expected, as introducing the micro-polar effect should not break the symmetry of the boundary value problems in pure Mode I loading. Interestingly, the higher-order constitutive responses have a profound impact on the crack propagation direction in the Mode II simulations. As shown in Fig. 6, the micropolar
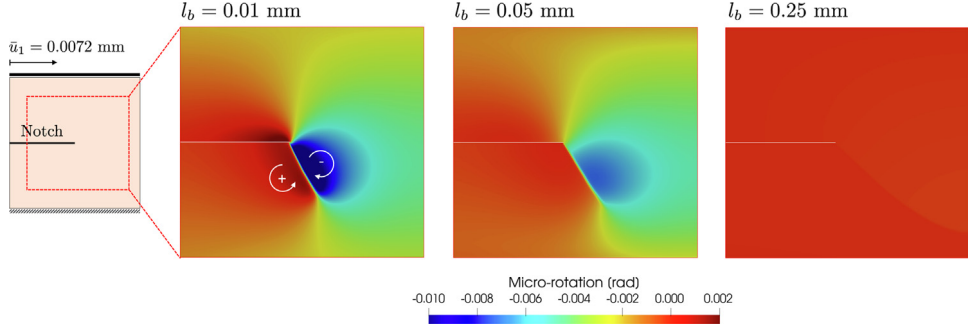
Fig. 7. Resultant micro-rotation field for single edge notched shear tests where $\bar{u}_1 = 0.0072$ mm.

(a) Global response from the tension test.   **(b)** Global response from the shear test.
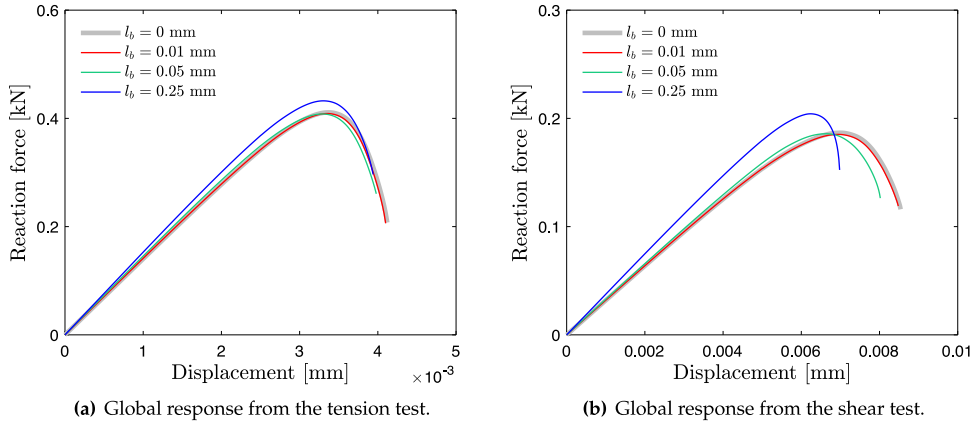
Fig. 8. The force–displacement curves from the single edge notched tests with regularization length $l_c = 0.008$ mm.

effect leads to a propagation direction bends counterclockwise. As the driving force for the phase field is affected by the micro-rotation induced by the coupling between shear and micro-rotation, this affects the energy dissipation mechanism and ultimately the energy minimizer of the action functional that provides the deformed configuration and crack patterns.

As pointed out in [36], the particles near crack tip resist micro-rotation and separation (i.e., interlocking), and the crack propagation mechanism in micropolar continuum therefore consists of the following steps. First, micro-rotational bonding between adjacent particles at the crack tip breaks and the particles starts to rotate with respect to each other. Second, the particles then move apart and the adjacent set of particles become the next crack-tip particles. Based on the mechanism, the crack path that minimizes the effort on breaking the micro-rotational bond (i.e., the path that maximizes the dissipation) is equivalent to the shortest path towards the boundary if the material is isotropic and homogeneous (e.g., a horizontal crack growth from the notch tip for the pure tensile loading case). The observed crack patterns shown in Fig. 6 are consistent with this interpretation. Furthermore, Fig. 6 also provides evidence to support that the non-polar model is a special case of the micropolar model in which $l_b \approx 0$. With a sufficiently small bending characteristic length l_b, the difference in crack patterns for the non-polar and micropolar cases is negligible. The coupling and the micro-rotational parts (ψ_e^C and ψ_e^R) then become significant enough to play a bigger role for crack growth as the bending characteristic length l_b increases.

As illustrated in Fig. 7, separated particles tend to rotate in opposite directions since they are no longer interlocked after crack formation. By revisiting Eq. (7) and Eq. (13), notice that the material constant γ that relates the fictitious undamaged couple stress $\bar{\boldsymbol{m}}^R$ to the micro-curvature $\bar{\boldsymbol{\kappa}}$ is proportional to the square of the characteristic lengths. The relationship implies that larger characteristic length leads to higher rigidity of the micropolar material, so that the separated particles tend to experience greater micro-rotation with smaller bending characteristic length.

Fig. 8 shows the load–deflection curves obtained from both tension and shear tests. The colored curves indicate the results with nonzero l_b, whereas the transparent gray curves denote the non-polar case. Since the force stress can
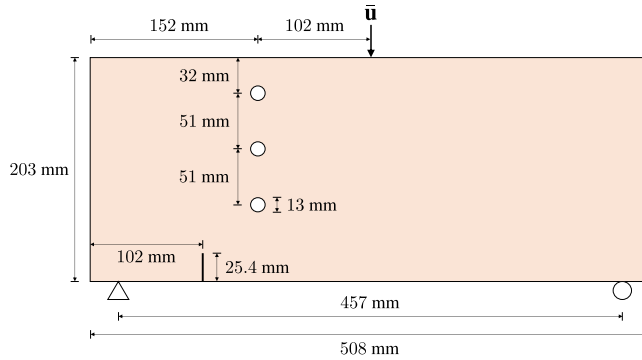
Fig. 9. Schematic of geometry and boundary conditions for the three-point bending tests.

be decomposed into two parts, e.g., $\bar{\sigma} = \bar{\sigma}^B + \bar{\sigma}^C$, micropolar material that possesses a large characteristic length tend to exhibit stiffer response compared to those with smaller characteristic lengths, due to the micro-continuum coupling effect. Unlike the tension test results in Fig. 8(a), the reaction forces reach their peak values under different strain level from the shearing tests [Fig. 8(b)]. This again highlights that the micropolar bending characteristic length affects the crack pattern, which in turn reflects different global response for the same boundary value problem.

5.3. Asymmetric notched three-point bending tests

This section examines a problem originally designed by Ingraffea and Grigoriu [75], which involves a three-point bending of a specimen with three holes. The domain of the problem is illustrated in Fig. 9. Since previous studies [10,43,75,76] have shown that different crack patterns can be observed depending on the notch depth and its position, we only focus on the case where the notch depth is set to be 25.4 mm.

We consider a specimen composed of a micropolar material and choose Boltzmann material parameters close to the properties of Plexiglas specimen tested by Ingraffea and Grigoriu [75]: $E = 3.2$ GPa, $v = 0.3$, $\mathcal{G}_c = 0.31$ N/mm, $l_c = 1.0$ mm, and $\psi_{\text{crit}} = 7.5$ kJ/m^3. For this problem, we assume that all the energy density parts can be degraded, i.e., $\mathfrak{D} = \{B, C, R\}$, $\mathfrak{U} = \varnothing$.

Within the problem domain (Fig. 9), we first attempt to investigate the effect of coupling number on the crack trajectory by conducting multiple numerical tests with different values: $N = 0.1$, $N = 0.5$, and $N = 0.9$, while bending characteristic length is held fixed as $l_b = 10.0$ mm. The numerical simulation was conducted under a displacement-controlled regime where we keep the load increment as $\Delta\bar{u}_2 = -2.0 \times 10^{-4}$ mm.

Fig. 10 illustrates the crack trajectories obtained by numerical experiments with different coupling number N in comparison to the experimental result [75], while Fig. 11 shows the measured reaction forces as a function of crack-mouth-opening-displacement (CMOD). Similar to the experimental results in Fig. 10(a), numerical results [Fig. 10(b)–(d)] show that the cracks tend to deflect towards the holes, eventually coalescing with the intermediate one. However, taking a closer look at Fig. 10(b)–(d), one can observe the slight differences on the concavity of the crack topologies especially when the crack passes close to the bottom hole. As we highlighted in Section 5.2, the crack tends to propagate through the path where the energy that takes to break the micro-rotational bond is minimized. At the same time, based on Saint-Venant's principle, the crack trajectory can also be affected by the bottom hole due to an increase of the singularity [10]. In this specific platform, it can thus be interpreted that the crack propagation may result from the competition between the two, based on the obtained results. Since the material that possesses higher degree of micropolarity requires more energy to break the micro-rotational bond, the bottom hole effect on the crack trajectory becomes negligible as coupling number N increases [Fig. 10(b)–(d)]. In addition, Fig. 11 implies that if more energy is required to break the micro-rotational bond, it results in higher material stiffness in the elastic regime, supporting our interpretation.

We then conduct a brief sensitivity analysis with respect to the time discretization (i.e., prescribed displacement increment $\Delta\bar{u}_2$) within the same problem domain, while we set the coupling number to be $N = 0.9$ during the analysis. Fig. 12 illustrates the simulated crack patterns for asymmetrically notched beam with three holes,
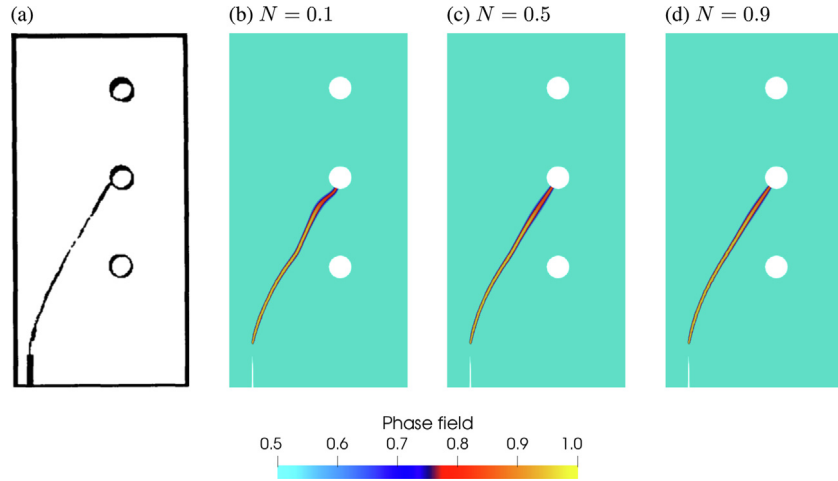
Fig. 10. Crack topologies for asymmetric notched three-point bending test: (a) experimentally obtained pattern by Ingraffea and Grigoriu [75]; (b)–(d) numerically obtained pattern with different coupling number N.
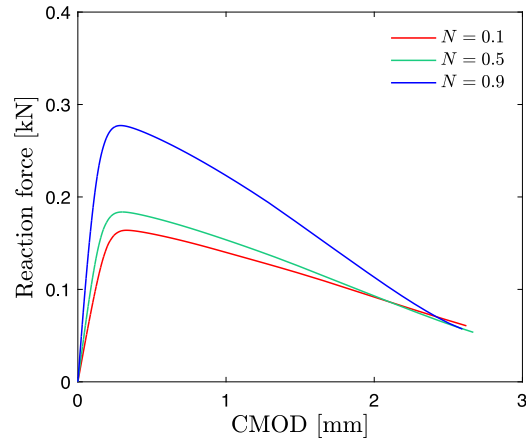

Fig. 11. Load–CMOD curves from the three-point bending test.
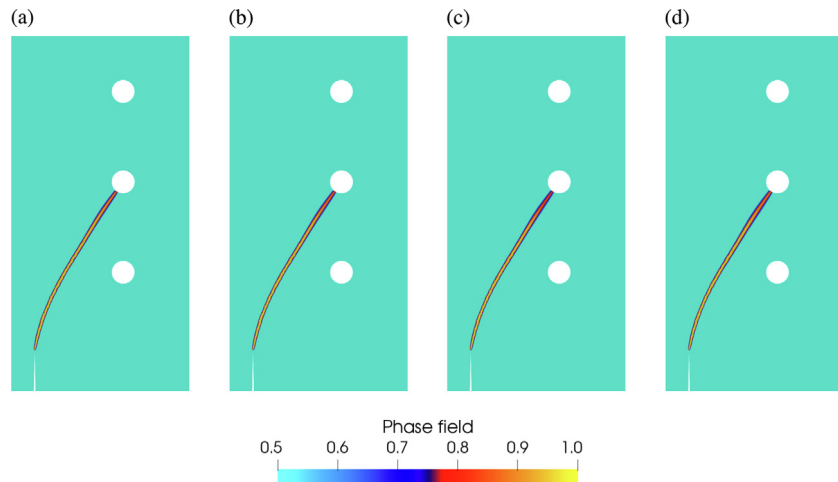
Fig. 12. Observed crack patterns for asymmetric notched three-point bending tests: (a) $\Delta \bar{u}_2 = -2.0 \times 10^{-4}$ mm; (b) $\Delta \bar{u}_2 = -4.0 \times 10^{-4}$ mm; (c) $\Delta \bar{u}_2 = -8.0 \times 10^{-4}$ mm; (d) $\Delta \bar{u}_2 = -16.0 \times 10^{-4}$ mm.
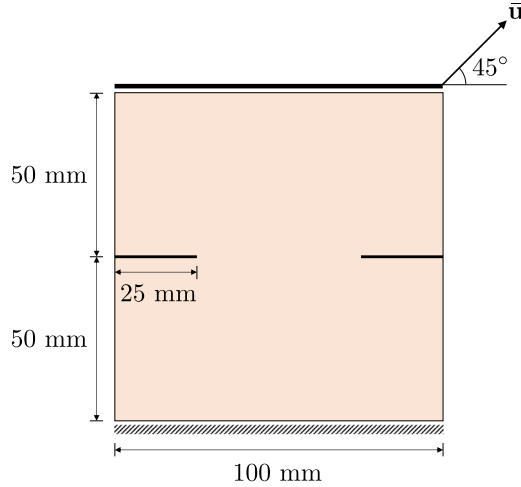
Fig. 13. Schematic of geometry and boundary conditions for the double edge notched tests.
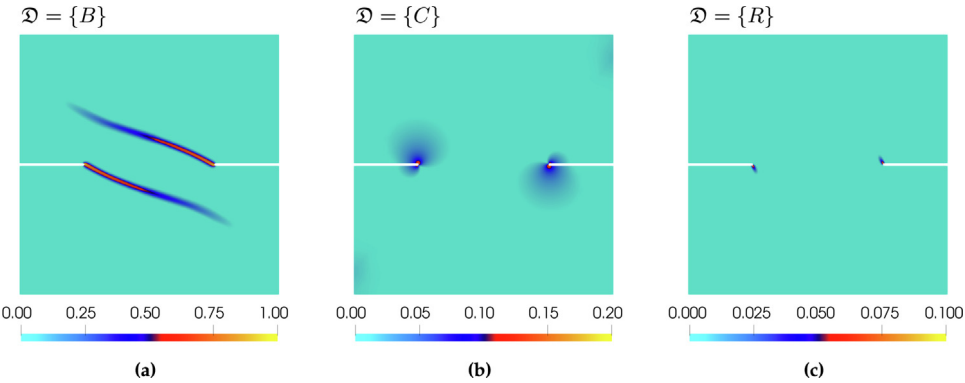
Fig. 14. Crack patterns for double edge notched tests obtained by considering different degradation functions [i.e., $g_i(d) = g(d)$ if $i \in \mathfrak{D}$; $g_i(d) = 1$ otherwise] on each energy density part, where $\bar{u}_1 = \bar{u}_2 = 0.05$ mm.

with different prescribed displacement rates, varying from $\Delta\bar{u}_2 = -4.0 \times 10^{-4}$ mm to -16.0×10^{-4} mm. Since meaningful differences in the crack trajectories are not observed, the result confirms the practical applicability of the explicit operator-splitting solution scheme, if the load increment is small enough.

5.4. Double edge notched tests

This numerical example investigates the effect of partial degradation of the strain energy density on the crack patterns. As illustrated in Fig. 13, the problem domain is a 100 mm wide and 100 mm long square plate with two 25 mm long symmetric initial horizontal edge notches at the middle. We assign the following material properties for this problem: $E = 30$ GPa, $\nu = 0.2$, $\mathcal{G}_c = 0.1$ N/mm, $l_c = 0.75$ mm, and $\psi_{\text{crit}} = 1.0$ kJ/m^3. Numerical experiments are simulated with bending characteristic length $l_b = 30.0$ mm and the coupling number is set to be $N = 0.5$. While the bottom part of the domain is held fixed, we prescribe the displacement along the entire top boundary at an angle of 45 degrees to the horizontal direction: $\Delta\bar{u}_1 = \Delta\bar{u}_2 = 5.0 \times 10^{-4}$ mm, such that the domain is subjected to combined tensile and shear loads.

Regarding partial degradation, recall Eq. (25) that energy density parts that correspond to the set $\mathfrak{U}$ remain completely undamaged, such that $g_i(d) = 1$ for $i \in \mathfrak{U}$, where $\mathfrak{D} \cup \mathfrak{U} = \{B, C, R\}$ and $\mathfrak{D} \cap \mathfrak{U} = \varnothing$. Within this platform, we first explore the effects of each individual energy density part by considering three different settings: (a) $\mathfrak{D} = \{B\}$; (b) $\mathfrak{D} = \{C\}$; and (c) $\mathfrak{D} = \{R\}$. Fig. 14 shows the fracture patterns occured in the double edge

$\mathfrak{D} = \{B\}$ $\mathfrak{D} = \{C\}$ $\mathfrak{D} = \{R\}$

(a) ψ_e^B in kJ/m^3 (b) ψ_e^C in kJ/m^3 (c) ψ_e^R in kJ/m^3
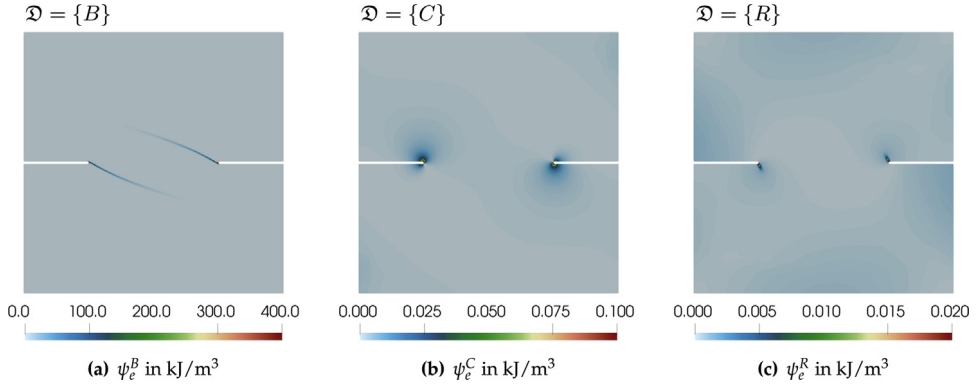
Fig. 15. Fictitious undegraded energy density part ψ_e^i ($i \in \mathfrak{D}$), where $\bar{u}_1 = \bar{u}_2 = 0.05$ mm.
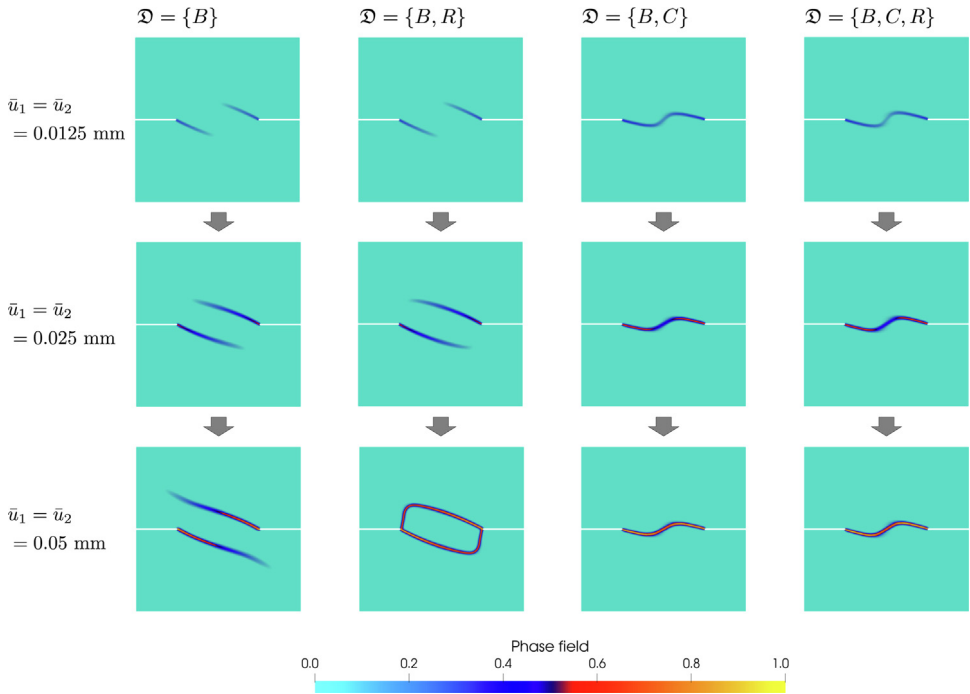
Fig. 16. Crack patterns for double edge notched tests with different combination of degrading energy density parts at several load increments.

notched tests for the three aforementioned cases where $\bar{u}_1 = \bar{u}_2 = 0.05$ mm. Under the same threshold energy density ψ_{crit}, the partial Boltzmann degradation case shown in Fig. 14(a) undergoes crack propagation, whereas degrading ψ_e^C [Fig. 14(b)] or ψ_e^R [Fig. 14(c)] exhibit only small amount of damage accumulation at the crack tip, without complete rupturing. It reveals that in either force or displacement-driven setup, most of the elastic energy is stored in the non-polar constituent; the amount of stored energy density parts: $\psi_e^B > \psi_e^C > \psi_e^R$. As illustrated in Fig. 15, only the fictitious undegraded Boltzmann energy density part locally exceeds the prescribed threshold $\psi_{\text{crit}} = 1.0$ kJ/m^3 through the cracks when $\mathfrak{D} = \{B\}$. Even though ψ_e^C and ψ_e^R do not exceed the threshold energy except the flaw tip region, the results also indirectly evidence that the coupling and pure micro-rotational energy density parts affect crack kinking, while the pure Boltzmann part mainly drives the crack to grow.

Since the pure Boltzmann part mainly drives the crack propagation, we now focus on the combined partial degradation with $B \in \mathfrak{D}$, also by considering three different settings within the same platform: (a) $\mathfrak{D} = \{B, R\}$; (b) $\mathfrak{D} = \{B, C\}$; and (c) $\mathfrak{D} = \{B, C, R\}$. Fig. 16 shows the crack patterns for double edge notched tests for three
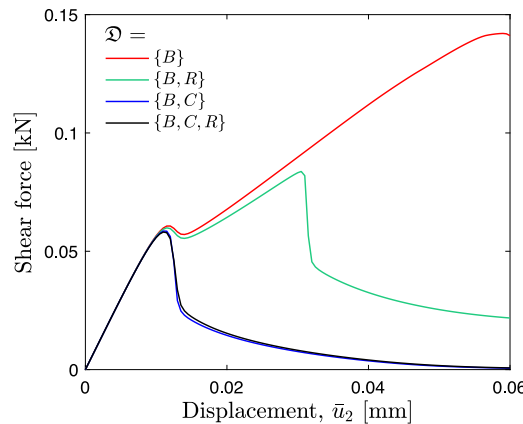
Fig. 17. The force–displacement curves from the double edge notched tests with different combination of degrading energy density parts.

different combinations of partial degradation compared with the case where $\mathfrak{D} = \{B\}$, while Fig. 17 illustrates the obtained load–deflection curves. The results confirm that degradation of the energy density parts ψ_e^C and ψ_e^R affects the crack kinking and curving.

The combined degradation with $\mathfrak{D} = \{B, R\}$ tend to stimulate similar fracture patterns compared to the partial Boltzmann degradation case until $\bar{u}_1 = \bar{u}_2 = 0.04$ mm, and then the cracks start to propagate towards the notches. Revisiting Fig. 15, this again indicates that the crack trajectories tend to follow the path that maximizes the energy dissipation (i.e., crack growth towards the adjacent flaw when the stored ψ_e^R at the tip becomes high enough). Similarly, the combined degradation with $\mathfrak{D} = \{B, C\}$ leads the cracks to grow towards the adjacent tip. In this case, however, the cracks tend to kink towards the adjacent notch from the beginning, and then two cracks coalescence toward each other after sufficient loading. Since the amount of stored coupling energy ψ_e^C is greater than the pure micro-rotational part ψ_e^R, we speculate that the coupling energy part influences the crack pattern more significantly compared to the micro-rotational energy part, so that we thus observe similar fracture pattern when $\mathfrak{D} = \{B, C, R\}$. In summary, this numerical experiment highlights that the pure Boltzmann energy density drives the crack growth, while the micro-continuum coupling energy density mainly influences the kinking direction.

6. Conclusion

This study presents a phase field fracture framework to model cohesive fracture in micropolar continua. To the best of the authors' knowledge, this is the first mathematics model that employs the phase field fracture framework to simulate crack growth in materials with size effect in both elastic and damaged regimes. To replicate the physical size effect for both the elastic deformation and crack growth, we split the elastic stored energy into the non-polar, coupling and micropolar components and introduce distinctive degradation mechanisms for them with regularization profiles that suppress the sensitivity of the phase field length scale parameter. One-dimensional analysis and numerical experiments demonstrate that the quasi-quadratic degradation function combined with linear local dissipation function suppresses the sensitivity of the length scale parameter for phase field while successfully incorporating the size effect with a length scale parameter that can be measured via standard inverse problems for micropolar materials. This feature may have significant implications for field-scale applications (e.g. geological formations, structural components) where the physical length scales of the materials are often much smaller than the mesh size and therefore the phase field length scale parameter.

Declaration of competing interest

The authors declare that they have no known competing financial interests or personal relationships that could have appeared to influence the work reported in this paper.

Acknowledgments

References

[1] Gilles A. Francfort, J.-J. Marigo, Revisiting brittle fracture as an energy minimization problem, J. Mech. Phys. Solids 46 (8) (1998) 1319–1342.

[2] Blaise Bourdin, Gilles A. Francfort, Jean Jacques Marigo, The variational approach to fracture, The Variational Approach to Fracture, ISBN: 9781402063947, 2008, http://dx.doi.org/10.1007/978-1-4020-6395-4.

[3] René de Borst, Clemens V. Verhoosel, Gradient damage vs phase-field approaches for fracture: Similarities and differences, Comput. Methods Appl. Mech. Engrg. 312 (2016) 78–94.

[4] Kun Wang, WaiChing Sun, A unified variational eigen-erosion framework for interacting brittle fractures and compaction bands in fluid-infiltrating porous media, Comput. Methods Appl. Mech. Engrg. 318 (2017) 1–32.

[5] Fadi Aldakheel, Blaž Hudobivnik, Ali Hussein, Peter Wriggers, Phase-field modeling of brittle fracture using an efficient virtual element scheme, Comput. Methods Appl. Mech. Engrg. 341 (2018) 443–466.

[6] Jian-Ying Wu, Vinh Phu Nguyen, A length scale insensitive phase-field damage model for brittle fracture, J. Mech. Phys. Solids 119 (2018) 20–42.

[7] Rudy J.M. Geelen, Yingjie Liu, John E. Dolbow, Antonio Rodríguez-Ferran, An optimization-based phase-field method for continuous-discontinuous crack propagation, Internat. J. Numer. Methods Engrg. 116 (1) (2018) 1–20.

[8] Eric C. Bryant, WaiChing Sun, A mixed-mode phase field fracture model in anisotropic rocks with consistent kinematics, Comput. Methods Appl. Mech. Engrg. (ISSN: 00457825) (2018) http://dx.doi.org/10.1016/j.cma.2018.08.008.

[9] Jinhyun Choo, WaiChing Sun, Cracking and damage from crystallization in pores: Coupled chemo-hydro-mechanics and phase-field modeling, Comput. Methods Appl. Mech. Engrg. 335 (2018) 347–379.

[10] Aurel Qinami, Eric Cushman Bryant, WaiChing Sun, Michael Kaliske, Circumventing mesh bias by r-and h-adaptive techniques for variational eigenfracture, Int. J. Fract. 220 (2) (2019) 129–142.

[11] Nima Noii, Fadi Aldakheel, Thomas Wick, Peter Wriggers, An adaptive global–local approach for phase-field modeling of anisotropic brittle fracture, Comput. Methods Appl. Mech. Engrg. 361 (2020) 112744.

[12] Nicolas Moës, John Dolbow, Ted Belytschko, A finite element method for crack growth without remeshing, Internat. J. Numer. Methods Engrg. 46 (1) (1999) 131–150.

[13] Francisco Armero, Christian Linder, New finite elements with embedded strong discontinuities in the finite deformation range, Comput. Methods Appl. Mech. Engrg. 197 (33–40) (2008) 3138–3170.

[14] Kun Wang, WaiChing Sun, A multiscale multi-permeability poroplasticity model linked by recursive homogenizations and deep learning, Comput. Methods Appl. Mech. Engrg. 334 (2018) 337–380.

[15] Kun Wang, WaiChing Sun, Meta-modeling game for deriving theory-consistent, microstructure-based traction–separation laws via deep reinforcement learning, Comput. Methods Appl. Mech. Engrg. 346 (2019) 216–241.

[16] Kun Wang, WaiChing Sun, An updated Lagrangian LBM–DEM–FEM coupling model for dual-permeability fissured porous media with embedded discontinuities, Comput. Methods Appl. Mech. Engrg. 344 (2019) 276–305.

[17] Stefan May, Julien Vignollet, Rene De Borst, A numerical assessment of phase-field models for brittle and cohesive fracture: γ-convergence and stress oscillations, Eur. J. Mech. A Solids 52 (2015) 72–84.

[18] Rudy J.M. Geelen, Yingjie Liu, Tianchen Hu, Michael R. Tupek, John E. Dolbow, A phase-field formulation for dynamic cohesive fracture, Comput. Methods Appl. Mech. Engrg. (ISSN: 00457825) (2019) http://dx.doi.org/10.1016/j.cma.2019.01.026.

[19] T.T. Nguyen, J. Yvonnet, M. Bornert, C. Chateau, K. Sab, R. Romani, R. Le Roy, On the choice of parameters in the phase field method for simulating crack initiation with experimental validation, Int. J. Fract. (ISSN: 1573-2673) 197 (2) (2016) 213–226, http://dx.doi.org/10.1007/s10704-016-0082-1.

[20] K.H. Pham, K. Ravi-Chandar, C.M. Landis, Experimental validation of a phase-field model for fracture, Int. J. Fract. 205 (1) (2017) 83–101.

[21] Jinhyun Choo, WaiChing Sun, Coupled phase-field and plasticity modeling of geological materials: from brittle fracture to ductile flow, Comput. Methods Appl. Mech. Engrg. 330 (2018) 1–32.

[22] Andreas Dietsche, Paul Steinmann, Kaspar Willam, Micropolar elastoplasticity and its role in localization, Int. J. Plast. 9 (7) (1993) 813–831.

[23] Zdenek P. Bazant, Jaime Planas, Fracture and Size Effect in Concrete and Other Quasibrittle Materials, Vol. 16, CRC press, 1997.

[24] Patrizia Trovalusci, Maria Laura De Bellis, Martin Ostoja-Starzewski, Agnese Murrali, Particulate random composites homogenized as micropolar materials, Meccanica 49 (11) (2014) 2719–2727.

[25] Kun Wang, WaiChing Sun, Simon Salager, SeonHong Na, Ghonwa Khaddour, Identifying material parameters for a micro-polar plasticity model via X-ray micro-computed tomographic (CT) images: lessons learned from the curve-fitting exercises, Int. J. Multiscale Comput. Eng. 14 (4) (2016).

[26] Fadi Aldakheel, A microscale model for concrete failure in poro-elasto-plastic media, Theor. Appl. Fract. Mech. 107 (2020) 102517.

[27] Jian-Ying Wu, Tushar Kanti Mandal, Vinh Phu Nguyen, A phase-field regularized cohesive zone model for hydrogen assisted cracking, Comput. Methods Appl. Mech. Engrg. 358 (2020) 112614.

[28] A. Cemal Eringen, Linear theory of micropolar elasticity, J. Math. Mech. (1966) 909–923.

[29] Nakamura Sachio, Robert Benedict, Roderic Lakes, Finite element method for orthotropic micropolar elasticity, Internat. J. Engrg. Sci. 22 (3) (1984) 319–330.

[30] W. Ehlers, W. Volk, On theoretical and numerical methods in the theory of porous media based on polar and non-polar elasto-plastic solid materials, Int. J. Solids Struct. 35 (34–35) (1998) 4597–4617.

[31] A. Cemal Eringen, Microcontinuum Field Theories: I. Foundations and Solids, Springer Science & Business Media, 2012.

[32] Elena Atroshchenko, Stéphane P.A. Bordas, Fundamental solutions and dual boundary element methods for fracture in plane cosserat elasticity, Proc. R. Soc. A 471 (2179) (2015) 20150216.

[33] Sara Grbčić, Adnan Ibrahimbegović, Gordan Jelenić, Variational formulation of micropolar elasticity using 3D hexahedral finite-element interpolation with incompatible modes, Comput. Struct. 205 (2018) 1–14.

[34] Eberhard Diegele, Rainer Elsäßer, Charalampos Tsakmakis, Linear micropolar elastic crack-tip fields under mixed mode loading conditions, Int. J. Fract. 129 (4) (2004) 309–339.

[35] Yong-Dong Li, Kang Yong Lee, Fracture analysis in micropolar elasticity: mode-i crack, Int. J. Fract. 156 (2) (2009) 179–184.

[36] A. Yavari, S. Sarkani, E.T. Moyer, On fractal cracks in micropolar elastic solids, J. Appl. Mech. 69 (1) (2002) 45–54.

[37] Roderic Lakes, W.J. Drugan, Bending of a Cosserat elastic bar of square cross section: theory and experiment, J. Appl. Mech. 82 (9) (2015) 091002.

[38] D. Bigoni, W.J. Drugan, Analytical derivation of Cosserat moduli via homogenization of heterogeneous elastic materials, J. Appl. Mech. 74 (4) (2007) 741–753.

[39] Patrizio Neff, Jena Jeong, Andreas Fischle, Stable identification of linear isotropic Cosserat parameters: bounded stiffness in bending and torsion implies conformal invariance of curvature, Acta Mech. 211 (3–4) (2010) 237–249.

[40] R.D. Mindlin, H.F. Tiersten, Effects of couple-stresses in linear elasticity, Arch. Ration. Mech. Anal. 11 (1) (1962) 415–448.

[41] R.D. Mindlin, Influence of couple-stresses on stress concentrations, Exp. Mech. 3 (1) (1963) 1–7.

[42] M. McGregor, M.A. Wheel, On the coupling number and characteristic length of micropolar media of differing topology, Proc. R. Soc. A 470 (2169) (2014) 20140150.

[43] Christian Miehe, Martina Hofacker, Fabian Welschinger, A phase field model for rate-independent crack propagation: Robust algorithmic implementation based on operator splits, Comput. Methods Appl. Mech. Engrg. (ISSN: 00457825) (2010) http://dx.doi.org/10.1016/j.cma.2010.04.011.

[44] Michael J. Borden, Clemens V. Verhoosel, Michael A. Scott, Thomas J.R. Hughes, Chad M. Landis, A phase-field description of dynamic brittle fracture, Comput. Methods Appl. Mech. Engrg. (ISSN: 00457825) (2012) http://dx.doi.org/10.1016/j.cma.2012.01.008.

[45] J.D. Clayton, J. Knap, Phase field modeling of directional fracture in anisotropic polycrystals, Comput. Mater. Sci. 98 (2015) 158–169.

[46] David Mumford, Jayant Shah, Optimal approximations by piecewise smooth functions and associated variational problems, Commun. Pure Appl. Math. 42 (5) (1989) 577–685.

[47] J.D. Clayton, J. Knap, Phase field modeling of twinning in indentation of transparent crystals, Modelling Simulation Mater. Sci. Eng. 19 (8) (2011) 085005.

[48] A. Mesgarnejad, B. Bourdin, M.M. Khonsari, Validation simulations for the variational approach to fracture, Comput. Methods Appl. Mech. Engrg. (ISSN: 00457825) (2015) http://dx.doi.org/10.1016/j.cma.2014.10.052.

[49] Jeremy Bleyer, Roberto Alessi, Phase-field modeling of anisotropic brittle fracture including several damage mechanisms, Comput. Methods Appl. Mech. Engrg. 336 (2018) 213–236.

[50] Christian Miehe, Fabian Welschinger, Martina Hofacker, Thermodynamically consistent phase-field models of fracture: variational principles and multi-field FE implementations, Internat. J. Numer. Methods Engrg. 83 (10) (2010) 1273–1311.

[51] Blaise Bourdin, Christopher J. Larsen, Casey L. Richardson, A time-discrete model for dynamic fracture based on crack regularization, Int. J. Fract. 168 (2) (2011) 133–143.

[52] Christian Miehe, M. Hofacker, L.-M. Schänzl, Fadi Aldakheel, Phase field modeling of fracture in multi-physics problems. Part II. Coupled brittle-to-ductile failure criteria and crack propagation in thermo-elastic–plastic solids, Comput. Methods Appl. Mech. Engrg. 294 (2015) 486–522.

[53] Christian Miehe, Lisa-Marie Schaenzel, Heike Ulmer, Phase field modeling of fracture in multi-physics problems. Part I. Balance of crack surface and failure criteria for brittle crack propagation in thermo-elastic solids, Comput. Methods Appl. Mech. Engrg. 294 (2015) 449–485.

[54] Chukwudi Chukwudozie, Blaise Bourdin, Keita Yoshioka, A variational phase-field model for hydraulic fracturing in porous media, Comput. Methods Appl. Mech. Engrg. 347 (2019) 957–982.

[55] Eric Lorentz, Sam Cuvilliez, Kyrylo Kazymyrenko, Modelling large crack propagation: From gradient damage to cohesive zone models, Int. J. Fract. (ISSN: 03769429) (2012) http://dx.doi.org/10.1007/s10704-012-9746-7.

[56] Eric Lorentz, A nonlocal damage model for plain concrete consistent with cohesive fracture, Int. J. Fract. 207 (2) (2017) 123–159.

[57] Carola Bilgen, Kerstin Weinberg, On the crack-driving force of phase-field models in linearized and finite elasticity, Comput. Methods Appl. Mech. Engrg. (ISSN: 00457825) (2019) http://dx.doi.org/10.1016/j.cma.2019.05.009.

[58] Kim Pham, Jean-Jacques Marigo, From the onset of damage to rupture: construction of responses with damage localization for a general class of gradient damage models, Contin. Mech. Thermodyn. 25 (2–4) (2013) 147–171.

[59] Christian Miehe, Steffen Mauthe, Stephan Teichtmeister, Minimization principles for the coupled problem of darcy–biot-type fluid transport in porous media linked to phase field modeling of fracture, J. Mech. Phys. Solids 82 (2015) 186–217.

[60] Eric Lorentz, Sam Cuvilliez, Kyrylo Kazymyrenko, Convergence of a gradient damage model toward a cohesive zone model, C. R. Méc. 339 (1) (2011) 20–26.

[61] Fabien Cazes, Anita Simatos, Michel Coret, Alain Combescure, A cohesive zone model which is energetically equivalent to a gradient-enhanced coupled damage-plasticity model, Eur. J. Mech. A Solids 29 (6) (2010) 976–989.

[62] Jian-Ying Wu, A geometrically regularized gradient-damage model with energetic equivalence, Comput. Methods Appl. Mech. Engrg. 328 (2018) 612–637.

[63] Ragnar Larsson, Yan Zhang, Homogenization of microsystem interconnects based on micropolar theory and discontinuous kinematics, J. Mech. Phys. Solids 55 (4) (2007) 819–841.

[64] Yan Zhang, Ragnar Larsson, Jing-yu Fan, Johan Liu, Interface modelling of microsystem interconnections using micropolar theory and discontinuous approximation, Comput. Struct. 85 (19–20) (2007) 1500–1513.

[65] Claudia Britta Hirschberger, Natarajan Sukumar, Paul Steinmann, Computational homogenization of material layers with micromorphic mesostructure, Phil. Mag. 88 (30–32) (2008) 3603–3631.

[66] Clemens V. Verhoosel, René de Borst, A phase-field model for cohesive fracture, Internat. J. Numer. Methods Engrg. 96 (1) (2013) 43–62.

[67] Timo Heister, Mary F. Wheeler, Thomas Wick, A primal-dual active set method and predictor-corrector mesh adaptivity for computing fracture propagation using a phase-field approach, Comput. Methods Appl. Mech. Engrg. 290 (2015) 466–495.

[68] S. Teichtmeister, D. Kienle, F. Aldakheel, M.-A. Keip, Phase field modeling of fracture in anisotropic brittle solids, Int. J. Non-Linear Mech. 97 (2017) 1–21.

[69] Anders Logg, Garth N. Wells, DOLFIN: Automated finite element computing, ACM Trans. Math. Softw. (TOMS) 37 (2) (2010) 20.

[70] Anders Logg, Kent-Andre Mardal, Garth Wells, Automated Solution of Differential Equations by the Finite Element Method: The FEniCS Book, Vol. 84, Springer Science & Business Media, 2012.

[71] Anders Logg, Garth N. Wells, Johan Hake, DOLFIN: A C++/Python finite element library, in: Automated Solution of Differential Equations by the Finite Element Method, Springer, 2012, pp. 173–225.

[72] Martin Alnæs, Jan Blechta, Johan Hake, August Johansson, Benjamin Kehlet, Anders Logg, Chris Richardson, Johannes Ring, Marie E. Rognes, Garth N. Wells, The FEniCS project version 1.5, Arch. Numer. Softw. 3 (100) (2015).

[73] Shrirang Abhyankar, Jed Brown, Emil M. Constantinescu, Debojyoti Ghosh, Barry F. Smith, Hong Zhang, Petsc/ts: A modern scalable ode/dae solver library, 2018, arXiv preprint arXiv:1806.01437.

[74] Hyoung Suk Suh, WaiChing Sun, An open-source FEniCS implementation of a phase field fracture model for micropolar continua, Int. J. Multiscale Comput. Eng. 17 (6) (2019) 639–663.

[75] Anthony R. Ingraffea, Mircea Grigoriu, Probabilistic Fracture Mechanics: A Validation of Predictive Capability, Technical report, Department of Structural Engineering, Cornell University, Ithaca, NY, 1990.

[76] R.U. Patil, B.K. Mishra, I.V. Singh, An adaptive multiscale phase field method for brittle fracture, Comput. Methods Appl. Mech. Engrg. 329 (2018) 254–288.